

AD-A213 168

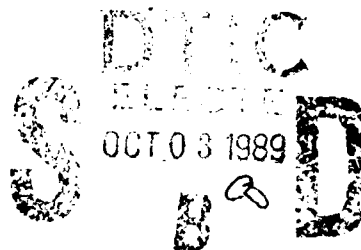
CHEMICAL  
RESEARCH,  
DEVELOPMENT &  
ENGINEERING  
CENTER

CRDEC-CR-045

SMALL PARTICLE SCATTERING AND ABSORPTION

Herschel Weil  
UNIVERSITY OF MICHIGAN  
Ann Arbor, MI 48109-2122

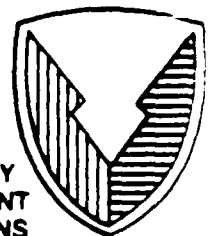
July 1989



DISTRIBUTION STATEMENT A

Approved for public release;  
Distribution Unlimited

U.S. ARMY  
ARMAMENT  
MUNITIONS  
CHEMICAL COMMAND



Aberdeen Proving Ground, Maryland 21010-5423

89 10 3 112

Disclaimer

The findings in this report are not to be construed as an official Department of the Army position unless so designated by other authorizing documents.

Distribution Statement

Approved for public release; distribution is unlimited.

REPORT DOCUMENTATION PAGE				Form Approved OMB No. 0704-0188	
1a. REPORT SECURITY CLASSIFICATION <b>UNCLASSIFIED</b>			1b. RESTRICTIVE MARKINGS		
2a. SECURITY CLASSIFICATION AUTHORITY			3. DISTRIBUTION/AVAILABILITY OF REPORT Approved for public release; distribution is unlimited.		
2b. DECLASSIFICATION/DOWNGRADING SCHEDULE					
4. PERFORMING ORGANIZATION REPORT NUMBER(S)  CRDEC-CR-045			5. MONITORING ORGANIZATION REPORT NUMBER(S)		
6a. NAME OF PERFORMING ORGANIZATION  University of Michigan		6b. OFFICE SYMBOL (If applicable)	7a. NAME OF MONITORING ORGANIZATION		
6c. ADDRESS (City, State, and ZIP Code)  Ann Arbor, MI 48109-2122			7b. ADDRESS (City, State, and ZIP Code)		
8a. NAME OF FUNDING/SPONSORING ORGANIZATION  CRDEC		8b. OFFICE SYMBOL (If applicable)  SMCCR-RSP-B	9. PROCUREMENT INSTRUMENT IDENTIFICATION NUMBER  DAAA15-86-K-0022		
8c. ADDRESS (City, State, and ZIP Code)  Aberdeen Proving Ground, MD 21010-5423			10. SOURCE OF FUNDING NUMBERS	PROGRAM ELEMENT NO.	PROJECT NO.
			TASK NO.	WORK UNIT ACCESSION NO.	
11. TITLE (Include Security Classification)  Small Particle Scattering and Absorption					
12. PERSONAL AUTHOR(S)  Weil, Herschel					
13a. TYPE OF REPORT  Contractor		13b. TIME COVERED FROM 86 Jun TO 88 Dec		14. DATE OF REPORT (Year, Month, Day)  1989 July	
15. PAGE COUNT  70					
16. SUPPLEMENTARY NOTATION  COR: Burt V. Bronk, SMCCR-RSP-B, (301) 671-3741					
17. COSATI CODES			18. SUBJECT TERMS (Continue on reverse if necessary and identify by block number) Light scattering, Bisphere. Internal energies. Raleigh particles.		
FIELD	GROUP	SUB-GROUP			
20	06				
19. ABSTRACT (Continue on reverse if necessary and identify by block number) An overview is given of the theoretical and computational research on electromagnetic scattering by small particles accomplished at the University of Michigan on CRDEC contract DAAA15-86-K-0022. Results that have been published in journal articles are described concisely. These include various special techniques to treat particles which are very thin compared to the incident wavelength, $L_0$ . Also in this group of published results, is a study of the internal, surface, and near fields for capped cylindrical particles, all of whose dimensions are small compared to $L_0$ and for which $L_0$ is in a wavelength range such as to excite plasmon or polariton resonances in the particle. Unpublished work along these lines is described in detail in an appendix. This more recent work considers the effects on the resonant modes of particle proximity and aggregation and also considers individual spheres with spherical holes either inside the spheres or forming bites in the sphere surface. The spheres with holes were studied at the suggestion of Dr. Burt Bronk. They are of particular interest in possible applications to catalysis of chemical reactions.					
20. DISTRIBUTION/AVAILABILITY OF ABSTRACT <input checked="" type="checkbox"/> UNCLASSIFIED/UNLIMITED <input type="checkbox"/> SAME AS RPT. <input type="checkbox"/> DTIC USERS			21. ABSTRACT SECURITY CLASSIFICATION <b>UNCLASSIFIED</b>		
22a. NAME OF RESPONSIBLE INDIVIDUAL  SANDRA J. JOHNSON			22b. TELEPHONE (Include Area Code)  (301) 671-2914		22c. OFFICE SYMBOL  SMCCR-SPS-T

UNCLASSIFIED

UNCLASSIFIED

## PREFACE

The work described in this report was authorized under Contract No. DAAA15-86-K-0022. This work was started in June 1986 and completed in December 1988.

The use of trade names or manufacturers' names in this report does not constitute an official endorsement of any commercial products. This report may not be cited for purposes of advertisement.

Reproduction of this document in whole or in part is prohibited except with permission of the Commander, U.S. Army Chemical Research, Development and Engineering Center, ATTN: SMCCR-SPS-T, Aberdeen Proving Ground, Maryland 21010-5423. However, the Defense Technical Information Center and the National Technical Information Service are authorized to reproduce the document for U.S. Government purposes.

This report has been approved for release to the public.



Accession For	
NTIC GRA1	<input checked="checked" type="checkbox"/>
DTIC TAB	<input type="checkbox"/>
Unannounced	<input type="checkbox"/>
Justification	
By	
Distribution/	
Availability Codes	
Dist	Avail and/or Special
A-1	

Blank

## CONTENTS

	Page
I. INTRODUCTION .....	7
II. THIN FLAT SCATTERERS: EXTENSION AND USE OF RESISTIVE SHEET BOUNDARY CONDITIONS .....	8
III. THIN FLAT SCATTERERS: FINITE THICKNESS DISKS .....	9
IV. ELECTRICALLY SMALL SCATTERERS; POLARITON AND PLASMON MODES .....	13
V. COMPUTER CODES .....	15
REFERENCES .....	19
APPENDIX: Resonances and Near and Internal Fields of Spheres with Cavities and Coagulated Spheres .....	21

Blank



## SMALL PARTICLE SCATTERING AND ABSORPTION

### I. INTRODUCTION

The aim of this contract is to extend our knowledge of the scattering and absorption of electromagnetic energy by aerosol particles.<sup>(1)</sup> Particular interest is in mm wave, infrared and optical scattering for particles of dimensions ranging from much smaller than to comparable with the incident wavelengths. The work proposed and accomplished was all theoretical and computational. Since the contract was terminated on short notice (as of May 31 1988) because of funding problems halfway through its 3 year intended life, not all the proposed research tasks in Sect. III of Ref. (1) and referred to in the progress reports were completed and some were not addressed at all. Nevertheless a considerable amount of work was successfully completed and the main results have been published in scientific journals<sup>[2]-[9],[12]\*</sup>, and/or been presented<sup>[13],[14]</sup> at the 1987 and 1988 CRDEC Scientific Conference on Obscuration and Aerosol Research. Ref. 14 will appear in the Proceedings of these Conferences and is reproduced here as an Appendix. In addition a number of Fortran computer codes developed on this contract have been provided to CRDEC on floppy discs along with additional documentation.

Some further work was done as part of a no-cost extension of the contract covering June 1988 - January 1989; for example, preparing the manuscripts for Reference 14 and extending the applicability and accuracy of the computer codes of Section V(3).

Sections II and III will summarize the papers.<sup>[2]-[9]</sup> They all deal with scattering and absorption by thin, flat, scatterers.

Some of our work described at the CRDEC conferences deals with particles which are not necessarily thin but which are small compared to the incident wavelengths. In particular, emphasis is on shape dependant absorption and near field effects in frequency bands corresponding to negative real part of the dielectric constant of the particle. This work, which we

\* Refs. 4-6 report on work done at the University of Michigan, but not supported by CRDEC contracts although related to the work on this contract.

describe in Section IV, was in progress at the time of the unexpected termination of the contract \* \* and had not yet been advanced to a state where we felt ready to publish as journal articles. We note, however, that it is an outgrowth of related work [12] accomplished under a predecessor CRDEC contract, DAAK11-82-K-0007.

The computer codes sent to CRDEC are implementations of solutions developed for some of the scattering and absorption problems described in Sections II-IV. The codes are described in Section V.

## II. THIN FLAT SCATTERERS: EXTENSION AND USE OF RESISTIVE SHEET BOUNDARY CONDITIONS

References 2-4 deal with techniques to solve scattering problems for thin scatterers by replacing them with idealized zero-thickness ( $t = 0$ ) sheets with thickness dependant resistivities and subject to jump boundary conditions for the electromagnetic fields. The reduction to  $t = 0$  sheets is done for infinite plane slabs of material irradiated by plane waves and allows only for a tangential surface current to be induced on the zero thickness sheet. The simulation becomes very inaccurate at oblique angles of incidence when the p-polarization component of the electric vector has a significant component normal to the layer and therefore induces a normal component of current density in the  $t \neq 0$  layer. In Ref. 2 this lack of a normal component for current density is rectified by superimposing on the resistive sheet a magnetically conductive sheet which can be interpreted as a covering of normally directed electric current dipoles. Ref. 2 derives this result from the limit  $t \rightarrow 0$  of the appropriate integral equations for the complete current density induced in the layer.

To apply modeling of a thin layer of infinite extent to real scatterers, which of course are of finite extent, is the concern of Refs. 3-7.\* In one approach the problem is attacked first by

\* Refs. 5 and 6 report on work done at the University of Michigan but not supported by CRDEC.

studying the diffraction by an edge of a  $t = 0$  half plane.<sup>[3],[4]</sup> In Ref. 5 an extension of these results to scattering by infinite thin strips of finite width is described.

A completely different approach is simply to neglect the edge effects on the current distribution and hence on the scattering cross-sections. The current density,  $\bar{J}$ , used is that of the infinite slab (or  $t = 0$  sheet) modified only by setting  $\bar{J} = 0$  for all points not in the layer (or sheet). This approach is referred to as a physical optics (PO) approximation.

In Ref. 6 this PO approximation coupled with the resistive sheet model was used to study back-scattering by a leaf. The theory applied to a rectangular scatterer was used to generate data to compare with laboratory measurements of a rectangular cutout from a coleus leaf. These show good agreement out to about an incidence angle of  $70^\circ$  from the normal to the leaf.

In Ref. 7 the PO approximation was used for thin disks but without modeling the finite thickness slab with a  $t = 0$  sheet;  $t$  was maintained in  $0 < kt \ll 1$ , where  $k = 2\pi/\text{incident wavelength}$  is the free space wave number.

The accuracy of the results by PO was explored in Ref. 7. We discuss this work in Section III. The reason for exploring the accuracy of PO lies in the principal use for single particle scattering results; namely in computation of radiation transfer through particle clouds. For this purpose it is necessary to average the scattering cross-sections over all orientations, sizes and shapes of the particles irradiated in the cloud. Clearly the simpler and faster the computation for each individual case in the averaging process, the better. PO results lead to simple, rapidly evaluated formulas whereas the accurate numerical methods such as CWW described in Section III require relatively heavy computation.

### **III. THIN FLAT SCATTERERS: FINITE THICKNESS DISKS**

A completely different technique than the zero thickness sheet methods of Section II is described in Ref (8) and (9). There the exact boundary value problem for thin circular disks is solved numerically by a combination of finite element and moment method techniques. This

method, which we have called CWW gives the internal and near fields as well as the far fields and can be used for materials from pure dielectrics to (almost) perfect conductors. Outputs can include bistatic, total, absorption and extinction cross sections, and also the current densities at all internal points. A thorough investigation in Ref. (8) of numerical results vs. experimental results as well as versus numerical results by an alternate technique and for special cases showed that the code CWW gives very accurate backscatter cross-sections for

$$0 \leq ka \leq 12$$

$$0 \leq kt \leq 0.5$$

$$1 < a/t \leq 10^4$$

where  $a$  and  $t$  are radius and thickness,  $k$  is free space wave number. There are no fundamental limits on the size of  $ka$  as far as the programmed formulas themselves are concerned, but the other two bounds are the results of approximations in the formulas. The computer code is discussed in Section V.

Two of the checks on CWW used in Ref. (8) are shown in Figure (1). These curves show, for a particular lossy dielectric disk, curves of the backscatter cross-section,  $\sigma$ , for circular incident polarization and the magnitude  $v$  and phase  $\Delta$  of the polarization ratio of the backscatter field.  $\sigma$  is normalized to the square of the wavelength and  $\theta$  is the angle of incidence relative to the normal to the flat disk surfaces. The curves compare results computed by CWW, by a very different Fredholm integral equation method Ref (10) and measured microwave experimental results Ref. (11).

Figure 2 shows comparisons of CWW and PO results as given by the equations derived in Ref. 7 and discussed in the paragraph below. For each disk the backscatter cross sections for p and s polarizations; that is for the incident electric field in the plane of the normal to the flat disk surface and the incident wave direction and perpendicular to this plane are labeled  $\sigma_{||}$  and  $\sigma_{\perp}$ . Curves of  $k^2\sigma_{||}$  and  $k^2\sigma_{\perp}$  versus angle of incidence  $\theta$  show how very close the results by the two methods can be.

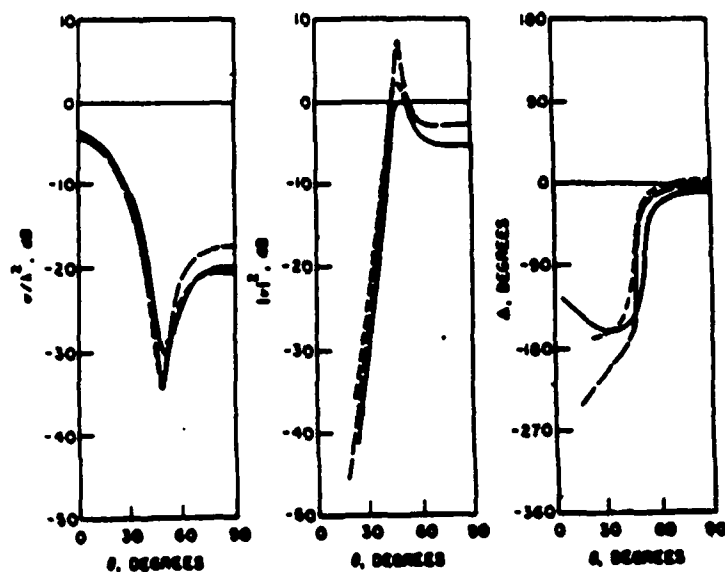


Figure 1. Comparison of computational results via CWW and via Shepard and Holt with Allan and McCormick experimental data for a disk of radius  $2.283\lambda$ , thickness  $0.460\lambda$ ,  $\epsilon = 3.13 + i 0.036$ : CWW solid line; Shepard and Holt, long dashes; experiment short dashes.

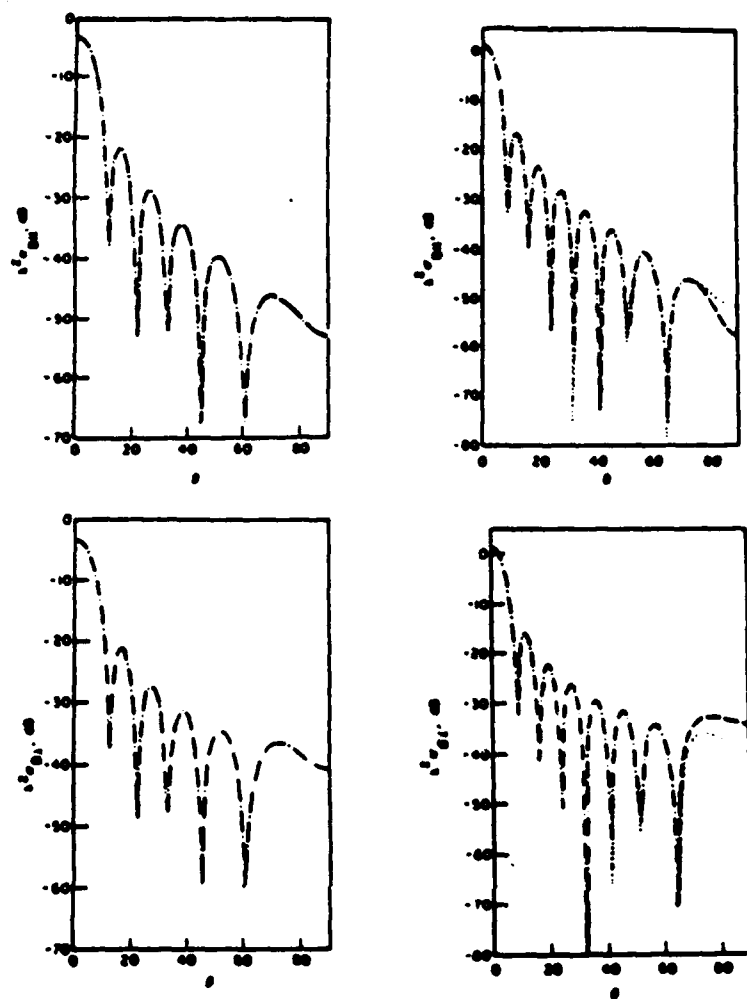


Figure 2. Comparison of principal plane cross sections vs. angle of incidence as computed by CWW (dashed lines) and by PO specialized for thin discs (dotted lines). For each case refractive index  $n = 2.0 + i0.01$ ;  $kt = 0.01$ ; (a)  $ka = 9.45$ , (b)  $ka = 12.57$ .

The CWW computations for a given disk and incident wave polarization and direction are, as we have already pointed out, sufficiently onerous that, for studying scattering and radiation transfer by clouds of disk-like scatterers with many different orientations and values of  $a$  and  $a/t$  it is desirable to have simple easily evaluated expressions. Simple analytic closed form expressions for the scattering cross sections of disks for the PO approximation with  $t \neq 0$  have been published and studied in several papers by D.M. Le Vine, of NASA Goddard, and colleagues. In Ref. (7), we have collaborated with Le Vine to compare results by PO with results by CWW for extensive series of physical situations. Criteria were thus established as to parameter ranges wherein one could use PO in lieu of CWW with adequate accuracy. This paper also contains a formulation of the PO formulas which is perhaps easier to follow than that in the earlier work by Le Vine and which shows up some unusual results as  $t \Rightarrow 0+$ . When  $|n|kt \ll 1$  ( $n$  = complex refractive index) this version of PO can be quite accurate even for very oblique incidence if  $a/t$  is large whereas the resistive sheet form of PO is not.

Contrary to what one might have expected the PO method (which neglects edge effects) does not necessarily become more accurate as radius  $a$  increases. In Figure 2(b) one notes that for both polarizations  $p$  and  $s$  the PO results deviate from CWW for  $\theta_D \gtrsim 65^\circ$  for  $ka = 12.57$ . When the thickness is reduced further the  $p$  component results become much more accurate all the way to  $90^\circ$  while the discrepancy remains for the  $s$  polarization. This loss of accuracy in PO results from the neglect of tangential circulating induced currents near the edges whereas significant circulating currents are computed by CWW and enter into the  $\sigma$  computations. Also at odds with what one might expect, PO is accurate for Rayleigh particles (as long as  $a/t \gg 1$ ). This is shown in Ref. 7.

#### IV. ELECTRICALLY SMALL SCATTERERS: POLARITON AND PLASMON MODES

Within the absorption bands of bulk dielectric materials and for wavelengths for metals where  $\text{Re } \epsilon < 0$  the internal fields are not pure e-m waves but are polariton and plasmon modes, the hybrid results of close coupling with internal vibrational and other wave modes. Within particles

small compared to the free space wavelength these internal fields can develop considerable structure and exhibit resonance behavior at specific shape dependent negative values of  $\text{Re } \epsilon$ . We have studied in some detail the effects of particle shape on these resonances; their frequencies and resulting narrow absorption lines and internal and near field structure. Ref. 12 studies these effects for hemispherically capped cylinders. Figure 3 from Ref. 12 shows an example of this structure and the concentration of the field near the surface of one of these cylinders. The equipotential and  $\bar{E}$  field lines are those induced by an incident  $\bar{E}$  field directed along the axis of rotation of the cylinder,  $x_3$ . The figure shows one quadrant in a plane through the  $x_3$  axis. Our more recent results cover much more general shapes such as spheres with holes in them, aggregations of spheres and disks, and rough surfaced particles. Some of these results are included in the Pierce and Weil presentations to the CRDEC conferences.<sup>[13(c)], [14]</sup> During the no cost extension period we continued this work (which is still in progress). Since the 1988 CRDEC Proceedings have not yet appeared we append Ref. 14 which outlines the theory and shows a number of results computed by codes described in Sect. V3.

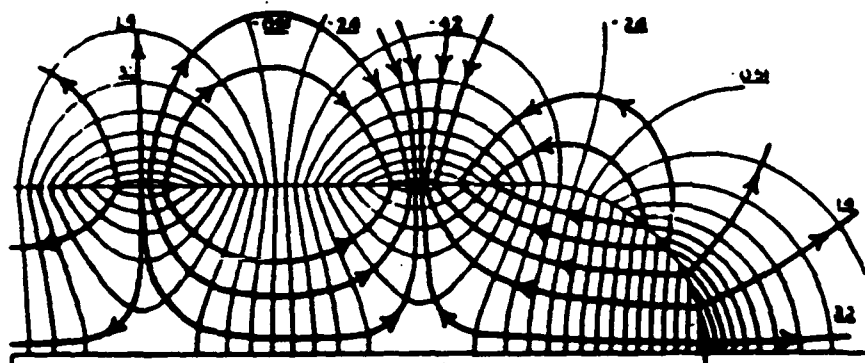


Figure 3. 4:1 Capped cylinder secondary resonance fields for incident potential  $\hat{x}_3$ :  $\epsilon = -1.740 + i 0.005$ ,  $\text{Re } V$ ,  $\Delta V = 1.86 \text{ V}$ . The imaginary field structure is similar, with  $\Delta V = 2.59 \text{ V}$ .



## V. COMPUTER CODES

The theoretical methods and formulas described in Sections III and IV have been implemented in various Fortran programs. The following codes were sent on floppy discs to CRDEC along with tutorials and sample results to help users get the codes running.

- (1) The programs used to obtain the CWW results for thin discs reported in Ref. (8) and (9) were sent in February 1987. These programs were intended to replace a slower and less accurate version which had been sent to CRDEC earlier. A copy of reference 9 was also sent; this reference gives much more detail of the theoretical basis for this material, the complete formulas programmed and the function of each program and subprograms. The programs are called

IGEN. FTN  
REGEN. FTN  
WMAIN. FTN  
ZMAIN. FTN  
WREAD. FTN  
ZSPLIT. FTN  
QNCS. FTN  
ZMEND. FTN  
CBLAS. FTN  
CSSLE. FTN  
XSECTS. FTN

These were all written by Thomas M. Willis. Data and other files to use with the tutorial and checking examples were also included.

- (2) Codes we developed to compute the scattered Stokes vector from clouds of disk and sphere scatterers for arbitrary distributions of size, orientation and material were also sent in February 1987 in a floppy disc. These programs are described globally in Ref. (15) but differ from the code actually used for Ref. (15) by incorporating the much improved and more accurate computation method CWW for individual disks. These programs, written

by Willis, are

CLOUDS. FTN  
SPHERES. FTN  
DISKS. FTN  
XSUBS. FTN

The PO formulas have not been added to this package of programs; this was one of the tasks we had intended to carry out.

- (3) Code to compute and plot the near and internal electric fields induced by electromagnetic waves incident on electrically small rotationally symmetric scatterers, was sent in January 1988. This code with some modification was used to generate the data in Ref. (14)\* and some of the data in Ref. 11(c). These programs are in FORTRAN 77 and are named

DIELMODE1. FTN  
ISO. FTN

They have been extended since January 1988 to be applicable and accurate for a wider class of particle shapes. A more detailed description of DIELMODE1.FTN and ISO.FTN plus related earlier code and the extensions since January follows. They were all developed by Leland Pierce.

There were three major programs developed by Mr. Pierce during this contract, as well as numerous graphics programs for display of final results. The three programs are all concerned with Rayleigh scattering from objects of various shapes and materials as described in the Appendix. The solution, in all cases, is for the static (zero frequency) potential, but with a value of complex dielectric constant that is the value for the material at the intended incident frequency of light. Since the main interest in this study is the resonant absorption by the particles, the light frequency is chosen to be in and around the frequencies where  $\epsilon$  has a negative real part and as

\* Ref. (14) is reproduced in the Appendix to this report.

small a non zero imaginary part as practical. (The exact theoretical locations of the resonances occur for  $\text{Im}\epsilon = 0$ .)

The three programs are variants of the same general program design, however each one is progressively more sophisticated in its capability and accuracy. The first explores the properties of two spherical particles: either near each other or coagulated more or less tightly. Here a sharp cusp in the surface of the coagulated particles is possible, and so more care was required in the numerical integration for the electric potential than had been done previously. Also, some completely new integration procedures were necessary due to the limitation of the previous code on non-reentrant bodies, i.e. those with depressions in their surfaces. Lastly, an error in the numerical integration routines that had gone undiscovered (though not unnoticed) for years was tracked down and fixed.

The second program DIELMODE consisted in a change of geometry, while still using circular arc segments to specify the outline of the particle. Here we faced a much more reentrant body than the first: spheres with spherical holes in them. There are many more shapes possible here than in the first program, but generally two canonical ones: a hole completely enclosed by the particle, which may be off-center; a spherical bite out of the side of the sphere. \* \* The new code development here required a new mesh for the local field calculations, and this was a major problem due to the geometry/mesh mismatch. Sub problems were that an interpolation method was needed for the potential at mesh points too close to the surface for accurate numerical integration and the isolines near the surface were drawn incorrectly due to an unsophisticated drawing algorithm. The interpolation problem was non-trivial, and so was tailored to work for this geometry only, while the isoline problem was avoided by oversampling with the mesh.

\* This generalization was suggested by Dr. Burt Bronk of CRDEC with the goal of applying the program to biological particles and catalysis.

This leads us now to the third and last program, which is nearing completion. This version is a final generalization for any particle shape that can be constructed out of circular arcs and straight line segments. This required a major effort to generalize the computation of whether a point was inside or outside the body, or on its surface. Also, many of the analytical integration formulas used for near-surface potential calculations had to be rederived for the most general cases, as well as derived for the first time for the straight line segments. Besides that, effort is still underway to develop a code to calculate the electric field with an integral equation, formulation, instead of the present finite difference technique, used to determine  $E$  from the potential. The finite difference method suffers at points near cusp-like discontinuities of the surface. The major development work here is the analytical integration of the singular and near singular terms, which for the electric field are more poorly behaved than for the potential.

The graphics programs developed include an x-y plotting package, an isoline plotting package (one for rectangular meshes (ISO.FTN) and another for polar-coordinate-type meshes), and a program to plot a function of two variables as a surface in three-dimensional space projected onto the paper at some viewing angle. All of these programs produce high-quality, fully-labelled plots on the computer screen or as black and white hardcopy through the use of a PostScript Apple LaserWriter.

## **REFERENCES**

These publications were all supported in part or entirely by contract DAAA15-86-K-00022 with the exception of Nos. 5 and 6.

1. H. Weil and T.B.A. Senior, Small Particle Scattering and Absorption- a three year research proposal, submitted to CRDEC by the Radiation Laboratory, Department of Electrical Engineering and Computer Science, University of Michigan, April 1986.
2. T.B.A. Senior and J.L. Volakis, "Sheet simulation of a Thin Dielectric Layer," *Radio Science* 22, pp. 1261-1272 (1987).
3. T.B.A. Senior, "A Critique of Certain Half-Plane Diffraction Analysis", *Electromagnetics* 1, pp. 81-90 (1987).
4. J.L. Volakis and T.B.A. Senior, "Diffraction by a Thin Dielectric Half Plane", *IEEE Trans. AP-35*, pp.1483-1487 (1987).
5. M. Herman and J.L. Volakis, "High Frequency Scattering by a Resistive Strip and Extensions to Conductive and Impedance Strips," *Radio Science* 22, pp. 335-349 (1987).
6. T.B.A. Senior, K. Sarabandi and F.T. Ulaby, "Measuring and Modeling the Backscattering Cross Section of a Leaf," *Radio Science* 22, pp. 1109-1116 (1987).
7. T.M. Willis, H. Weil and D.M. Le Vine, Applicability of Physical Optics Thin Plate Scattering, *IEEE Trans. on Geoscience and Remote Sensing*, 28, pp 153-160 (1988).
8. T.M. Willis and H. Weil, Disk Scattering and Absorption by an Improved Computational Method, *Applied Optics* 26, pp.3987-3995 (1987).
9. T.M. Willis and H. Weil, "Internal Induced Fields, Scattering and Absorption of Electromagnetic Radiation by Disk Shaped Aerosols; an Improved Computational Formulation and Computer Code", University of Michigan Memo RL 023618-1-T, Dec 1986.
10. J.W. Shepard and A.R. Holt, "The Scattering of Electromagnetic Radiation from Finite Dielectric Circular Cylinders," *J. Phys. A. Math. Gen.* 16, pp. 651-662 (1983).
11. L.E. Allan and G.C. McCormick, "Measurement as the Backscattered Matrix of Dielectric Bodies," *IEEE Trans. AP-28*, pp. 166-169 (1980).
12. H. Weil, T.B.A. Senior and T.M. Willis III, "Internal and Near Fields of Small Particles Irradiated in Spectral Absorption Bands," *J. Optical Soc. Am. A* 2, pp. 989-996 (1985).
13. To appear in the Proceedings of the 1987 CRDEC Scientific Conference on Obscuration and Aerosol Research:
  - (a) H. Weil and T.M. Willis, "Summary of Recent Work at the University of Michigan relevant to e-m wave scattering and absorption by small particles"

- (b) T.M. Willis and H. Weil, "Verification of Disk Scattering by the CWW (Full Wave) Method and Range of Validity"
  - (c) L. Pierce and H. Weil, "Absorption by Spheres and Aggregates of Spheres."
14. L. Pierce and H. Weil, "Resonances and Near and Internal Fields of Spheres with Cavities and Coagulated Spheres." To appear in the Proceeding of the 1988 CRDEC Scientific Conference on Obscuration and Aerosol Science: A slightly modified version of this paper constitutes the 1988 University of Michigan Report No. RL 023618-2-T and is included as an Appendix to the present report.
  15. H. Weil and T. M. Willis, "Model for Polarization Effects in Remote Probing of Clouds", Radio Science, 17, pp. 1018-1026, Sept. 1982.

## APPENDIX

**Resonances and Near and Internal Fields  
of Spheres with Cavities and Coagulated Spheres \***

Leland Pierce and Herschel Weil

The University of Michigan, Radiation Lab, EECS Dept.

Ann Arbor, MI 48109-2122

## ABSTRACT

Work in progress is reported on electromagnetic scattering and absorption from Rayleigh spheres that are coagulated and spheres that have cavities in them. Absorption cross-sections are calculated at frequencies around that of visible light, and static internal and near-field equipotential lines are plotted. Polarizability tensor elements are calculated and modeled for a few specific cases. The significance of these models in the context of absorption cross-sections is explored. Future work will concentrate on specific applications of this work to problems in the physical, chemical, and biological sciences.

## I. GENERAL FORMULATION

This paper explains the formulation and implementation of the low-frequency scattering problem as applied to some axially-symmetric homogeneous dielectric bodies. In particular two families of shapes are investigated:

1. Two spheres of equal dimension. Their center-to-center separation is variable, and hence produces two coagulated spheres or two complete spheres near each other.
2. Single sphere with a spherical cavity. Here the position and size of the cavity are variable, producing hollow spherical shells, off-center holes in spheres, and holes in the surface of the sphere.

To start with, both theory and practice are introduced for the general case. Later in this section the model for some of our results is presented and discussed. In section two the results for coagulated spheres are presented, while in section three the results for the sphere with cavity are presented. Section four summarizes the results and discusses future plans.

#### 1a. Theory

The work we present is an extension of the investigation described by Weil [1986]. It follows the formulation of Rayleigh theory given by Senior [1976] (see fig. 1.1). The polarization tensor  $P_{ij}$  and the dipole moments  $p_i$  of the induced fields:

$$p_i = \epsilon_0 P_{ij} E_j$$

are found by considering the fields in the limit as  $k_0 \rightarrow 0$ . Hence one solves the statics problem of figure 1.1.

Let  $\Phi_j^e$  be the scattered, exterior potential and  $\Phi_j$  be the total, interior potential. Then the conditions governing  $\Phi_j^e$  and  $\Phi_j$  for a unit electric field excitation of a scatterer of boundary B and unit outward normal  $\hat{n}$  are:

$$\nabla^2 \Phi_j^e = 0 \quad \text{Outside B}$$

$$\Phi_j^e = O(r^{-2}) \text{ as } r \rightarrow \infty$$

$$\nabla^2 \Phi_j = 0 \quad \text{Inside B}$$

$$\Phi_j^e = \Phi_j + x_j \quad \text{On B}$$

$$\frac{\partial}{\partial n} \Phi_j^e = \epsilon \frac{\partial}{\partial n} \Phi_j + \hat{n} \cdot \hat{x}_j \quad \text{On B}$$

By using Green's Theorem twice, once inside and once outside B, and combining the results,



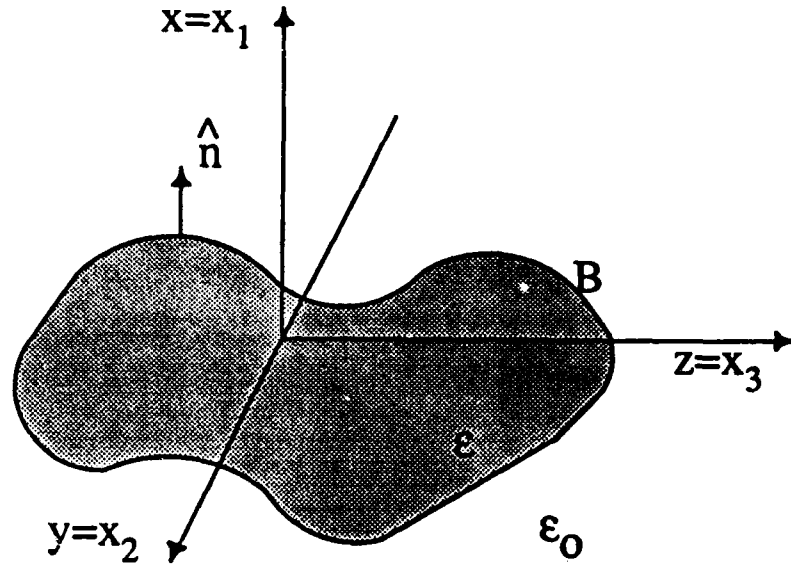


Figure 1.1 — Geometry of the Scattering Problem.

Senior obtained: \*

$$\Gamma[\Phi_j^i + x_j] + (1 - \Gamma)[\epsilon \Phi_j + x_j] = \frac{(1 - \epsilon)}{4\pi} \int_B (\Phi_j^i - x_j') \frac{\partial}{\partial n'} \left( \frac{1}{R} \right) dS'$$

where  $R = |\bar{r} - \bar{r}'|$ , and

$$\Gamma = \begin{cases} 1, & \text{if } \bar{r} \text{ is external to } B \\ \frac{1}{2}, & \text{if } \bar{r} \text{ is on } B \\ 0, & \text{if } \bar{r} \text{ is interior to } B \end{cases}$$

Now specialize to a body of revolution in cylindrical coordinates  $\rho, \phi, z$ :

$$dS' = \rho' d\phi' ds'$$

where  $s'$  is length along the body perimeter,  $S$ .

For an  $x$ -directed  $\bar{E}$  field the right hand side becomes:

$$= \frac{(1 - \epsilon)}{4\pi} \int_0^{2\pi} \int_S (\Phi_1^i - x') \frac{\partial}{\partial n'} \left( \frac{1}{R} \right) \rho' d\phi' ds'$$

Since the total field will vary as  $\cos\phi'$ , along the body's perimeter it can be written in the form:

$$\Phi_1^i = \Phi_1^i - x' = \frac{-1}{1 - \epsilon} W_1(s') \cos\phi'$$

\* This is the correct form of the corresponding equation which is given following eq. 19 in Senior (1976)

so the right hand side becomes

$$= -\frac{1}{4\pi} \int_S \left[ \int_0^{2\pi} \cos\phi' \frac{\partial}{\partial n'} \left( \frac{1}{R} \right) d\phi' \right] W_1(s') \rho' ds'$$

Senior and Ahlgren [ 1972, eqn. 63, p. 20 ] put this expression into the form:

$$= -\frac{1}{4\pi} \int_S 2\cos\phi \{ \rho \cos\alpha' \Omega_2 + [(z' - z) \sin\alpha' - \rho' \cos\alpha'] \Omega_1 \} W_1(s') \rho' ds'$$

At  $\phi = 0^\circ$  this gives:

$$\left. \begin{array}{l} \text{outside:} \quad -\Phi_1^t(\bar{r}) \\ \text{bndry: } \frac{1}{2} \frac{(1+\epsilon)}{(1-\epsilon)} W_1(s) \\ \text{inside:} \quad -\epsilon \Phi_1(\bar{r}) \end{array} \right\} = \rho + \frac{1}{2\pi} \int_S W_1(s') \{ \rho \cos\alpha' \Omega_2 + [(z' - z) \sin\alpha' - \rho' \cos\alpha'] \Omega_1 \} \rho' ds'$$

This is an integral equation for  $W_1$  when  $\bar{r}$  is on the surface B. Similarly for the z-directed  $\bar{E}$  field excitation, the field along the body's perimeter can be written in the form:

$$\Phi_3^t = \frac{-1}{1-\epsilon} W_3(s')$$

$$\left. \begin{array}{l} \text{outside:} \quad -\Phi_3^t(\bar{r}) \\ \text{bndry: } \frac{1}{2} \frac{(1+\epsilon)}{(1-\epsilon)} W_3(s) \\ \text{inside:} \quad -\epsilon \Phi_3(\bar{r}) \end{array} \right\} = z + \frac{1}{2\pi} \int_S W_3(s') \{ \rho \cos\alpha' \Omega_1 + [(z' - z) \sin\alpha' - \rho' \cos\alpha'] \Omega_0 \} \rho' ds'$$

In these equations

$$\Omega_n = \int_0^\pi \frac{\cos^n(\Psi)}{R^3} d\Psi \quad n = 0, 1, 2$$

and

$$R = [(\rho + \rho')^2 + (z - z')^2] [1 - m \sin^2 \theta]$$

where

$$m = \frac{4\rho\rho'}{(\rho + \rho')^2 + (z - z')^2}$$

$$\theta = \frac{1}{2}(\pi - \Psi)$$

Senior and Ahlgren ( p. 61 ) show that

$$\Omega_0 = \frac{1}{4} \left( \frac{m}{\rho\rho'} \right)^{3/2} \left[ K(m) + 2m \frac{d}{dm} K(m) \right]$$

$$\Omega_1 = \left( \frac{m}{\rho\rho'} \right)^{3/2} \left[ \left(1 - \frac{m}{2}\right) \frac{d}{dm} K(m) - \frac{1}{4} K(m) \right]$$

$$\Omega_2 = \frac{1}{m^2} \left( \frac{m}{\rho\rho'} \right)^{3/2} \left[ 2m \left(1 - \frac{m}{2}\right)^2 \frac{d}{dm} K(m) - \left(1 - \frac{m^2}{4}\right) K(m) + E(m) \right]$$

where K and E are Elliptic Integrals.

The Electric Polarizability Tensor is

$$P_{ij} = (1 - \epsilon_r) \int_B \hat{n} \cdot \hat{x}_i \Phi_j dS$$

For the case of rotational symmetry about the z-axis  $P_{11} = P_{22} \neq 0$ ;

$P_{33} \neq 0$ ;  $P_{ij} = 0, i \neq j$ . Hence we need only find  $P_{11}$  and  $P_{33}$ .

The absorption cross-section can be expressed in terms of  $P_{ii}$ , and by averaging over all possible scatterer orientations ( all assumed equally likely ) one gets the average absorption cross-section:

$$\langle \sigma_A \rangle = \frac{k_0 V}{3} \text{Im.}(2P_{11} + P_{33})$$

where  $k_0$  is the free-space wavenumber of the incident light, and V is the volume of one scatterer. The dimensionless quantity  $\langle \sigma_A \rangle / k_0 V$  is used in the plots of absorption vs. wavelength presented later.

## Ib. Practice

The integral equations for  $W_1$  and  $W_3$  are solved using the moment method. We choose pulse basis functions and delta-function weighting functions to get a point-matching solution.

The body perimeter is broken up into equal-length arcs and the  $W$ 's are determined at the center of each arc. The integral becomes:

$$\int_{s'} W_i(s') K_i(\bar{r}, \bar{r}') \rho' ds' = \sum_{j=1}^N W_i(s_j) \int_{s_j-\Delta/2}^{s_j+\Delta/2} K_i(\bar{r}, \bar{r}') \rho' ds'$$

where  $j$  runs over every segment of the perimeter, and  $i$  is either 1 or 3.

A simple six-point integration scheme works well if  $\bar{r}$  is on the surface, and the surface has no cusps. However, to get the near fields, and accurate surface values for complicated shapes, a more sophisticated method must be used. This is because for  $\bar{r}$  near the surface  $K(\bar{r}, \bar{r}')$  varies rapidly, hence a 6-point integration scheme will not capture it sufficiently.

Our method removes the rapidly-varying terms and integrates them analytically over the appropriate very small sub-segment (approximating it as straight, no longer curved). This can give us accurate field values near the surface and elsewhere.

The numerically troublesome terms are in the  $\Omega_n$ 's. Specifically a  $\frac{1}{m_1}$  term and a  $\ln(\frac{1}{m_1})$  term. Both blow up as the field point approaches the surface (source point) in our integral equations. Since

$$\begin{aligned} K(m) &\simeq (a_0 + a_1 m_1 + \dots + a_4 m_1^4) \\ &\quad + (b_0 + b_1 m_1 + \dots + b_4 m_1^4) \ln\left(\frac{1}{m_1}\right) \\ \frac{d}{dm} K(m) &\simeq \left(\frac{b_0}{m_1} + (b_1 - a_1) + (b_2 - 2a_2)m_1 + \dots + (b_4 - 4a_4)m_1^3\right) \\ &\quad - (b_1 + 2b_2 m_1 + \dots + 4b_4 m_1^3) \ln\left(\frac{1}{m_1}\right) \end{aligned}$$

$$E(m) \simeq 1 - \frac{1}{4} m_1 + \frac{1}{4} m_1 \ln\left(\frac{1}{m_1}\right)$$

where  $m_1 = 1 - m$ . The troublesome terms are:

$$\begin{aligned} \frac{b_0}{m_1} & \text{ in the } \frac{d}{dm} K(m) \text{ term,} \\ -b_1 \ln\left(\frac{1}{m_1}\right) & \text{ in the } \frac{d}{dm} K(m) \text{ term,} \\ \text{and } b_0 \ln\left(\frac{1}{m_1}\right) & \text{ in the } K(m) \text{ term.} \end{aligned}$$

The constants  $a_i$  and  $b_i$  can be found in Abramowitz and Stegun [1964]. We pulled these terms out of the expressions for  $K_i(\bar{r}, \bar{r}')$ , integrated them analytically, then added them back in to the numerical integration which was done with the remaining terms.

The geometry to explain the following formulas for the analytic evaluations is shown in figure 1.2.

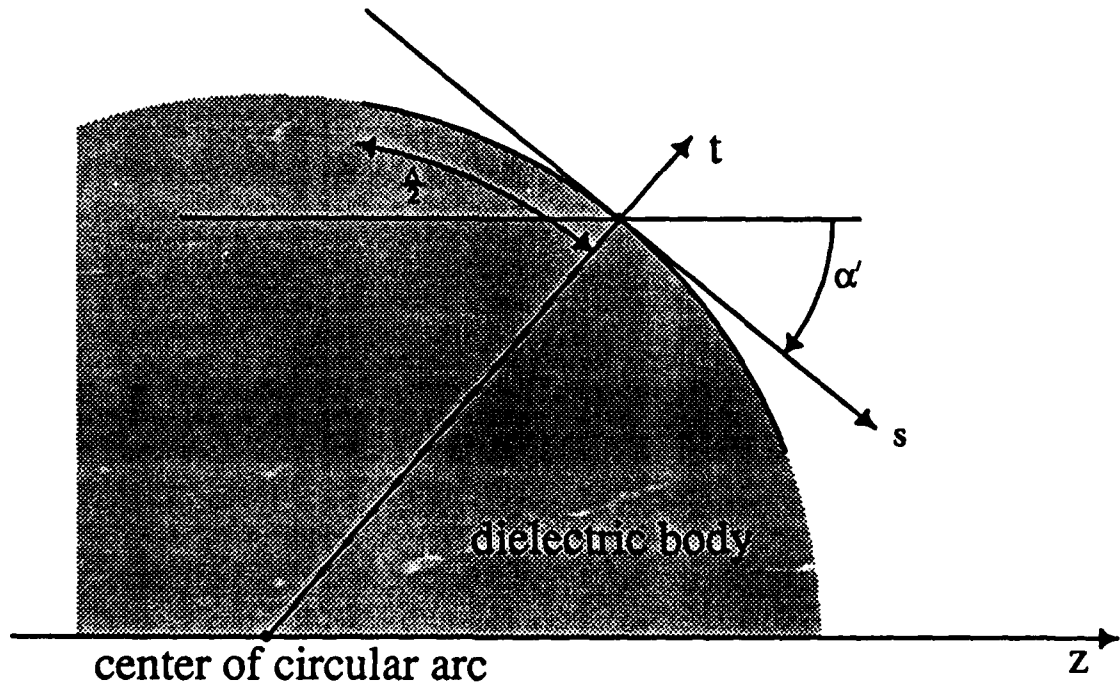


Figure 1.2 — Coordinates used for Surface Integration.

We need to evaluate two integrals involving  $b_o/m_1$ :

$$I_1 = \int_{-\frac{\Delta}{2}}^{\frac{\Delta}{2}} \frac{1}{m_1} ds' = 2 \sin \alpha' (s \sin \alpha' + t \cos \alpha') \ln \left[ \frac{\Delta^2/4 - s\Delta + s^2 + (t' - t)^2}{\Delta^2/4 + s\Delta + s^2 + (t' - t)^2} \right] + \Delta$$

$$+ \frac{4(s \sin \alpha' + t \cos \alpha')(s \sin \alpha' + t' \cos \alpha')}{t' - t} \left[ \tan^{-1} \left( \frac{\Delta - 2s}{2(t' - t)} \right) + \tan^{-1} \left( \frac{\Delta + 2s}{2(t' - t)} \right) \right]$$

$$I_2 = \int_{-\frac{\Delta}{2}}^{\frac{\Delta}{2}} \frac{s'}{m_1} ds' =$$

$$(s \sin \alpha' + t \cos \alpha') \left\{ (4s \sin \alpha' + 2t' \cos \alpha') \ln \left[ \frac{\Delta^2/4 - s\Delta + s^2 + (t' - t)^2}{\Delta^2/4 + s\Delta + s^2 + (t' - t)^2} \right] + 4\Delta \sin \alpha' \right.$$

$$\left. + \frac{4[st' \cos \alpha' + s^2 \sin \alpha' - (t' - t)^2 \sin \alpha']}{t' - t} \left[ \tan^{-1} \left( \frac{\Delta - 2s}{2(t' - t)} \right) + \tan^{-1} \left( \frac{\Delta + 2s}{2(t' - t)} \right) \right] \right\}$$

These integrals are combined with the other terms in the expressions for the  $\Omega_n$ 's and then with others to make the  $K_i$ 's. The following expressions are for that part of each  $K_i$  that is singular:

$$K_{1,extra} = \frac{2[s^2 + t^2 + t'^2 + 2t' \sin \alpha' (s \cos \alpha' - t \sin \alpha')]}{t' [s^2 + (t + t')^2 + 4t' \sin \alpha' (s \cos \alpha' - t \sin \alpha')]^{5/2}}$$

$$\cdot (s^2 + t^2 - t'^2) [t' \cos \alpha' I_1 + \sin \alpha' I_2]$$

$$K_{3,extra} = \frac{4 \cos \alpha' [s \sin \alpha' + t \cos \alpha'] [s^2 + t^2 - t'^2]}{[s^2 + (t + t')^2 + 4t' \sin \alpha' (s \cos \alpha' - t \sin \alpha')]^{5/2}} [t' \cos \alpha' I_1 + \sin \alpha' I_2]$$

The analysis is similar for the  $\ln(m_1)$  term.

### Ic. Polarizability Tensor Elements

The calculation of absorption spectra is useful and desirable by itself, however, a more theoretically satisfying calculation that can yield much deeper insight into absorption spectra of irregularly shaped particles is that of  $P_{ii}$  as a function of  $\epsilon$ , instead of frequency and material. Cast in this way, there is a direct analogy with the analytical formula for a sphere. For a Rayleigh sphere we have:

$$\text{Im.}(P_{11}) = \frac{9\epsilon_r''}{(\epsilon_r' + 2)^2 + \epsilon_r''^2}$$

where  $\epsilon_r'$  and  $\epsilon_r''$  are the real and imaginary parts, respectively, of the complex relative permittivity of the sphere. This can intuitively be seen as a sharp resonance of "strength" 9 at  $\epsilon_r' = -2$ , which stands out against a more uniform background; see fig 1.3. Physically, this resonance can be explained as a coupling of electromagnetic energy into an internal, non-electromagnetic vibrational mode of the material: the electromagnetic energy is used to drive the lattice vibrations. In dielectric materials this mode is called a polariton, whereas in metals a similar excited mode is called a surface plasmon [Nelson, 1979].

Expressions similar to those for the sphere be given for ellipsoids [see Bohren and Huffman, p.350]. Using this idea, we can reformulate the numerical procedure to give us the eigenvalues of the integral equation. The resonant positions ( $\epsilon_r'$  to give infinite absorption when  $\epsilon_r'' = 0$ ) are then simple functions of these eigenvalues. Using these resonant  $\epsilon$ 's and some numerically-generated  $\text{Im.}P_{ii}(\epsilon)$ , we can fit this data with a generalization of the preceding formula; ie:

$$\text{Im.}P_{ii}(\epsilon) = \sum_{k=1}^N \frac{A_k \epsilon_r''}{(\epsilon_r' - \epsilon_{res,k})^2 + \epsilon_r''^2}$$

This procedure works quite well. The only problem with it is that the decision concerning  $N$  is difficult: the discretized version of the integral equation has as many eigenvalues as the size of the matrix we create. Which of these are "real"? So far, we have chosen those resonances that are most prominent for large  $\epsilon_r''$ . Sometimes this leaves out certain resonances that are numerically quite prominent when  $\epsilon_r''$  is small, but decay rapidly with increasing  $\epsilon_r''$ . However, most of the resonances don't even get this far: they have no peak near the negative real  $\epsilon$  axis; hence, they are assumed to be due to the discretization process.

Absorption as a function of Complex Relative Permittivity ( $\epsilon_r$ ), sphere

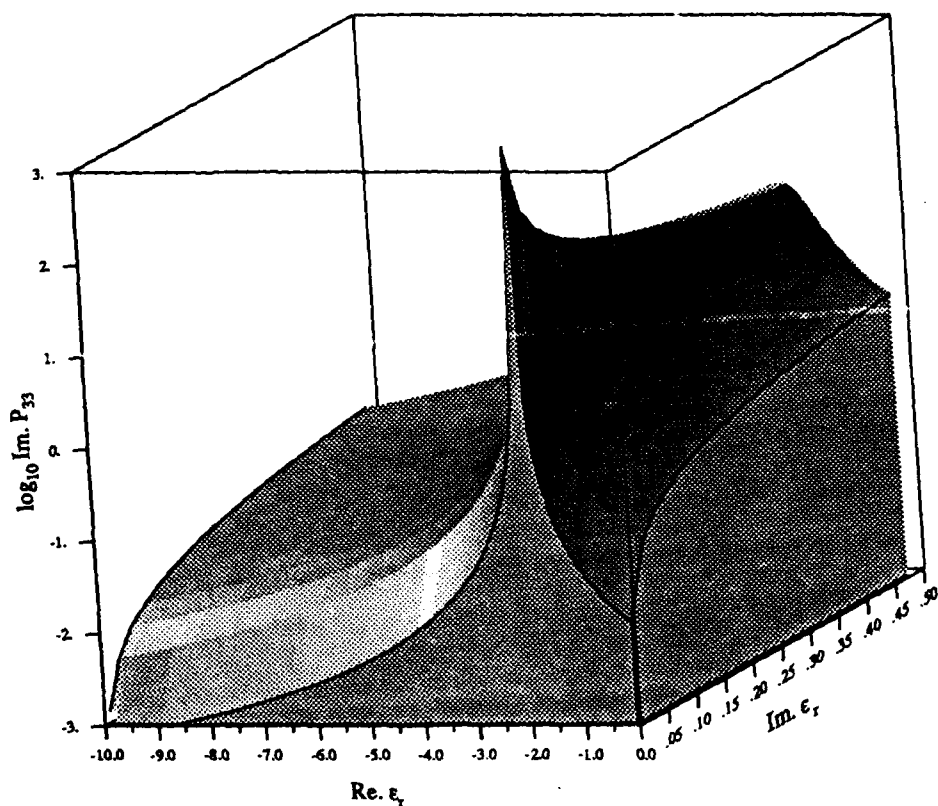


Figure 1.3 — Analytical Im.(Polarisability) for a Sphere

So far, the resonances that decay quickly are also thought of as spurious, but more analysis in the future may reveal a different explanation. Illustrations of this for the particular shapes investigated here are included in sections two and three.



## II. COAGULATED SPHERE RESULTS

We simulated two spheres, both separate and coagulated. Two examples are the following:

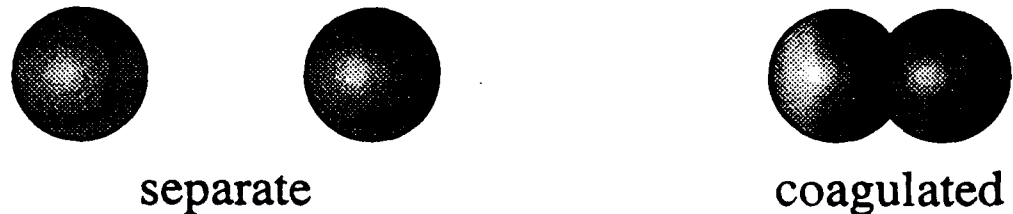


Figure 2.1 — Two examples from the family of sphere pairs

The center-to-center separation of the two spheres is given in terms of the sphere diameter. For example, the separate spheres above have a center-to-center separation of about 2, whereas the two coagulated spheres have a center-to-center separation of about 0.8. This is made more plain in figure 2.2.

The fields were plotted with a variety of separations and also at many different frequencies; each different frequency corresponds to a different  $\epsilon$  for gold, tabulated in Physik Daten [ 1981 ]. Due to symmetry, only a portion of the field structure is shown. That part of the field that intersects the plane through the symmetry axis (see fig 2.3) and is in the first quadrant (darkened piece of the plane) is displayed in the field plots. The wire mesh is meant to represent the surface of the (see-thru) particle that is being halved by the cutting plane.

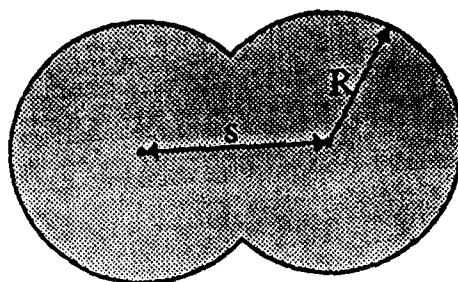
Typical field plots are shown in figs 2.4–2.7 for the near-resonance case and for the off-resonance case. Each of the field plots has the real part and imaginary part of the potential for a particular shape, frequency and 'incident' E-field direction:

x-directed means E is vertical at infinity.

z-directed means E is horizontal at infinity.

Each plot has 4–6 equipotential lines, while  $\Delta V$  (or "spacing in volts" on the plots) between them varies from plot-to-plot. Hence a large value for  $\Delta V$  means that we have high local E-field concentrations.

Tau in each plot is the value for the relative dielectric constant.



$R = 0.5$  - radius of solid sphere  
 $s$  = center-to-center separation

### EXAMPLES





$s=0.0$  -- a sphere:   
 $s=0.5$  -- 2 intersecting spheres:   
 $s=1.0$  -- 2 just-touching spheres:   
 $s=2.0$  -- 2 separate spheres: 

Figure 2.2 — The coagulated sphere geometry

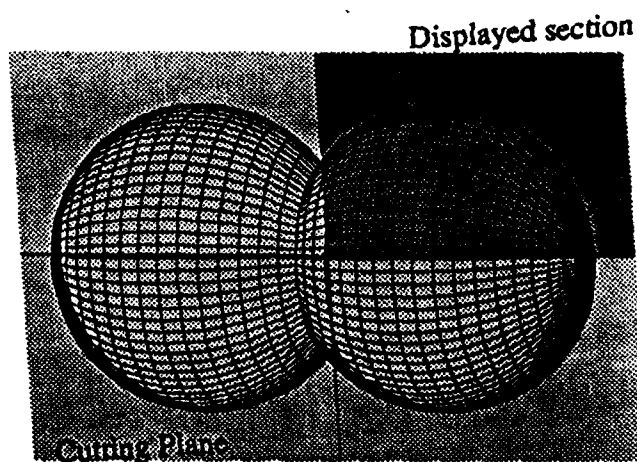
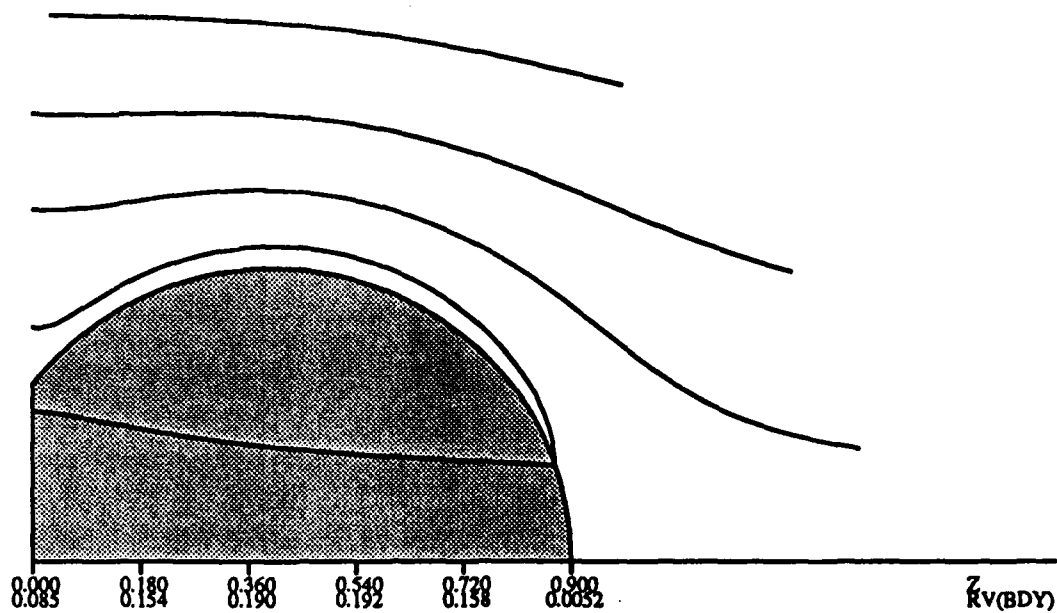


Figure 2.3 — Position of field plots in relation to the particle

The dimensionless average absorption cross-section, as described earlier, was plotted for each geometry as a function of free-space wavelength. Typical spectra are shown in figs 2.8-2.17.

X DIRECTED EXCITATION REAL PART  
 $\tau = 0.960$   
 SPACING IN VOLTS = 0.24605  
 $R_{V\min}(\text{VOLT}) = -0.78913$   
 $R_{V\max}(\text{VOLT}) = 0.19507$

\*\*\*\*\* ISO-RV CURVES \*\*\*\*\*  
 $R_V = -0.666, -0.420, -0.174, 0.07204,$   
 Center-to-Center Spacing: 0.8000



X DIRECTED EXCITATION IMAGINARY PART  
 $\tau = 0.960$   
 SPACING IN VOLTS = 0.00691  
 $I_{V\min}(\text{VOLT}) = 0.00000$   
 $I_{V\max}(\text{VOLT}) = 0.02763$

\*\*\*\*\* ISO-IV CURVES \*\*\*\*\*  
 $I_V = .00345, .01036, .01727, .02417,$   
 Center-to-Center Spacing: 0.8000

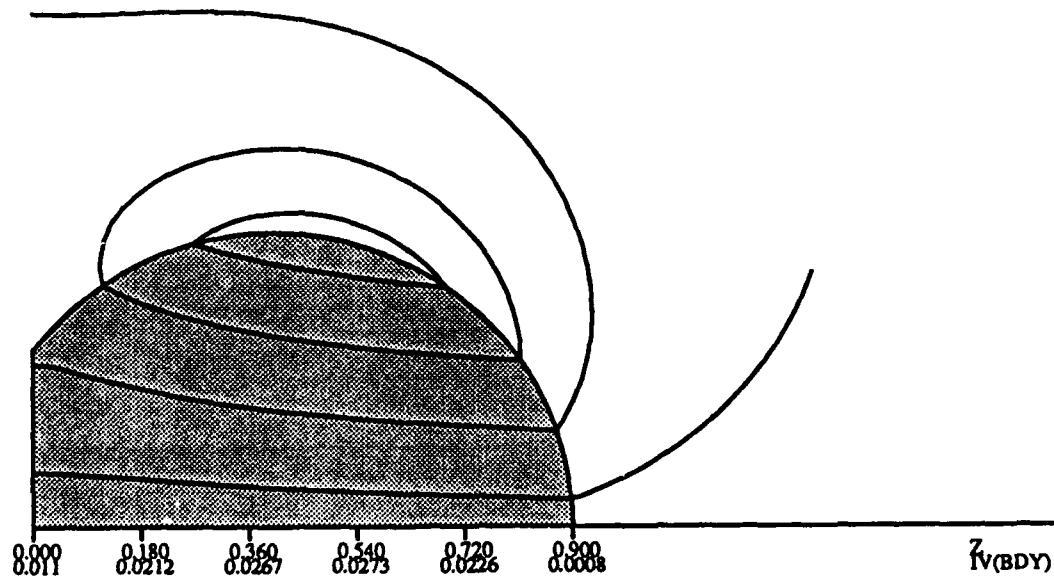


Figure 2.4 — Iso-Potential Lines for Near-Resonance Case (x-inc.)

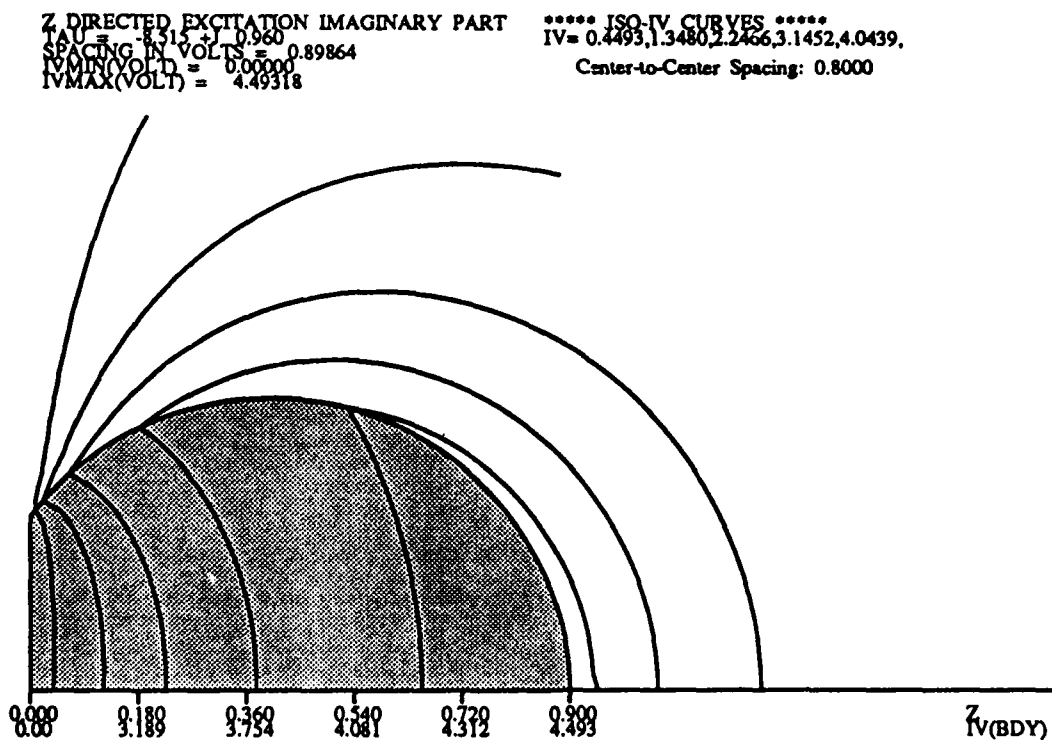
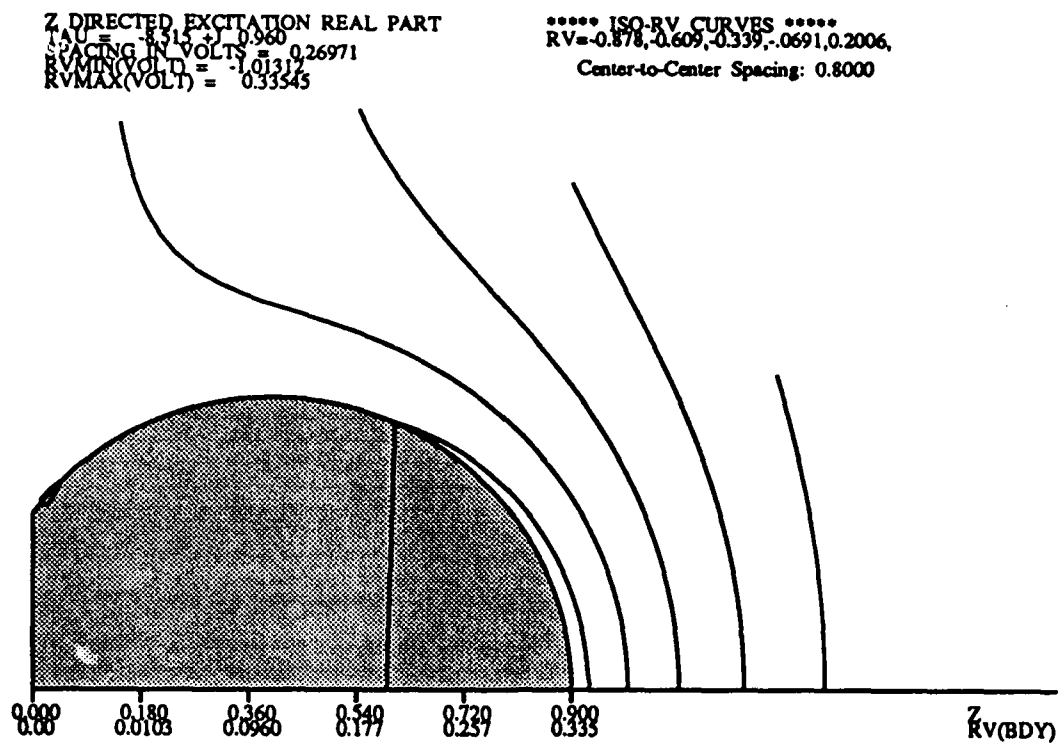
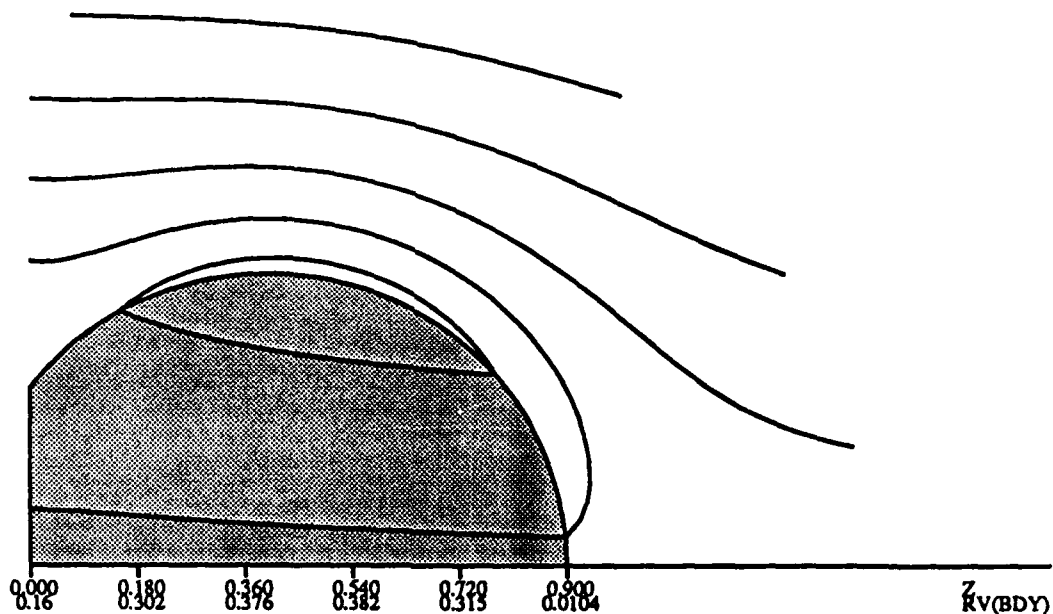


Figure 2.5 — Iso-Potential Lines for Near-Resonance Case ( $z$ -inc.)

X DIRECTED EXCITATION REAL PART  
 $\tau_{AU} = -1.390 + j1.480$   
 SPACING IN VOLTS = 0.22419  
 $RV_{MIN}(VOLT) = -0.73333$   
 $RV_{MAX}(VOLT) = 0.38761$

\*\*\*\*\* ISO-RV CURVES \*\*\*\*\*  
 $RV = -0.621, -0.397, -0.173, 0.05132, 0.2755,$   
 Center-to-Center Spacing: 0.8000



X DIRECTED EXCITATION IMAGINARY PART  
 $\tau_{AU} = -1.390 + j1.480$   
 SPACING IN VOLTS = 0.04329  
 $IV_{MIN}(VOLT) = 0.00000$   
 $IV_{MAX}(VOLT) = 0.21646$

\*\*\*\*\* ISO-IV CURVES \*\*\*\*\*  
 $IV = 0.02163, 0.06494, 0.1082, 0.1515, 0.1948,$   
 Center-to-Center Spacing: 0.8000

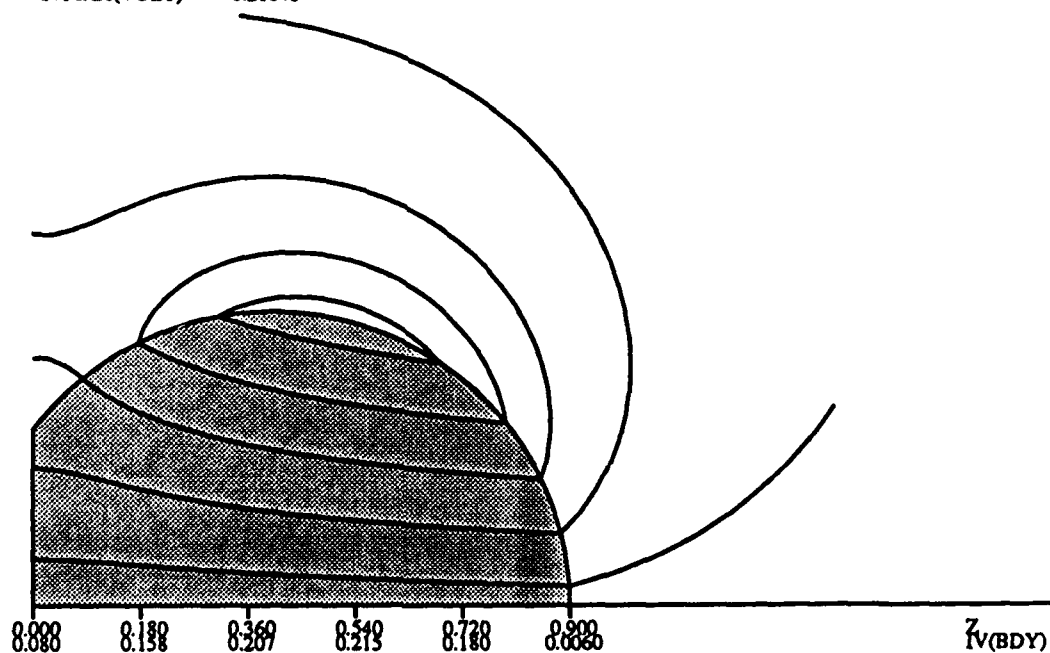


Figure 2.6 — Iso-Potential Lines for Off-Resonance Case (x-inc.)

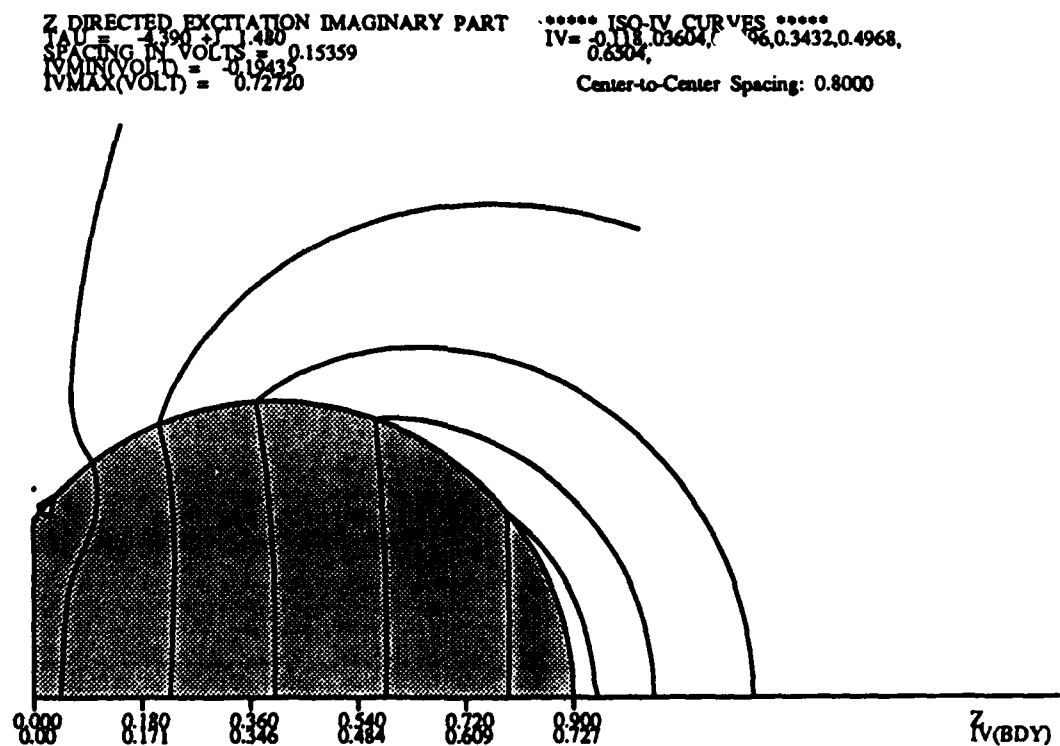
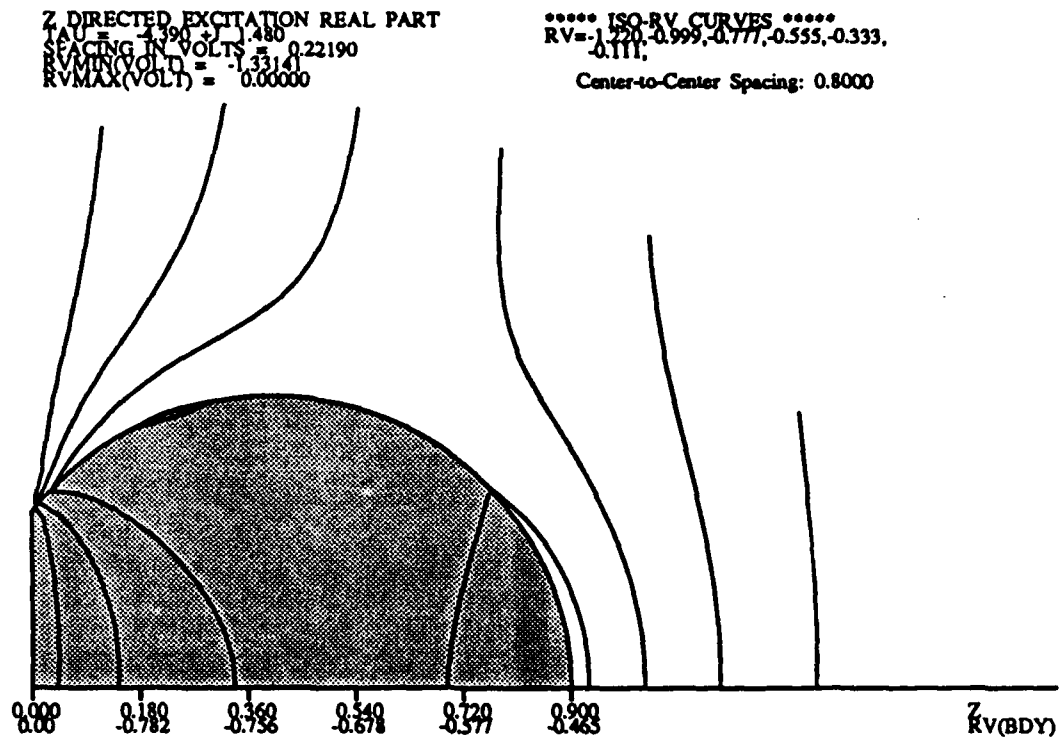


Figure 2.7 — Iso-Potential Lines for Off-Resonance Case (z-inc.)

In comparing the near- and off-resonance fields, note that the resonance itself is numerically apparent in the voltage magnitudes of the resonant  $z$ -directed imaginary part: an increase of slightly less than five times. This resonance is for the  $z$ -directed excitation only. The field structure for the  $x$ -directed cases changes very little. One notable difference is that the field strength in the imaginary parts ( $x$ -dir) becomes about ten times smaller as compared to the off-resonance case. This is interesting and deserves further investigation to determine if it is a general feature or just a specific occurrence.

Moving on to a comparison of the  $z$ -directed field plots, the most striking difference is in the field structure: the resonant field lines are much more curved. A consequence of this is that the near-surface electric field is much stronger and the internal field is much weaker: hence the term "surface mode" for this kind of resonance behavior. There are a number of other distinguishing features of these field plots, but their significance is undetermined at this time: the "chimney" in the real part has moved from an off-center position off-resonance to, apparently, the central position of the particle; the field concentration at the central cusp of the particle has moved from the real part off-resonance to the imaginary part near-resonance.

The following pages show the absorption spectrum of coagulated gold particles in the frequency range near that of visible light. Note that the vertical scales are different, and that the absorption spectrum for a single sphere is included in each plot for comparison. Recall that 'sep' in these plots stands for the center-to-center separation between the two spherical particles that make up the coagulated particle. A separation of 1.0 indicates that the two spheres are just barely touching one another, while a separation of 0.8 indicates that the two spheres are overlapping and are coagulated. A separation greater than one indicates that the two spheres are near each other but not touching.

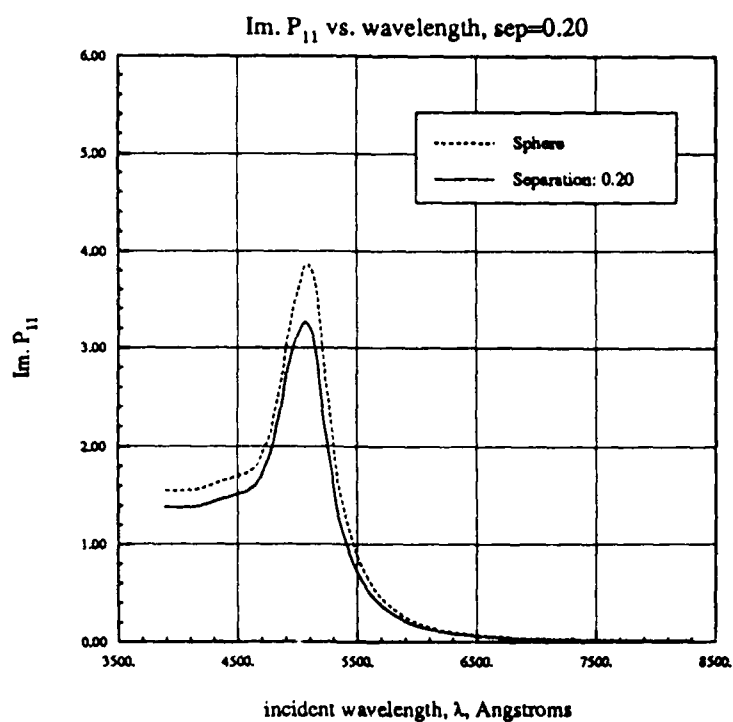


Figure 2.8 — X-Incidence Absorption Spectrum, sep=0.2

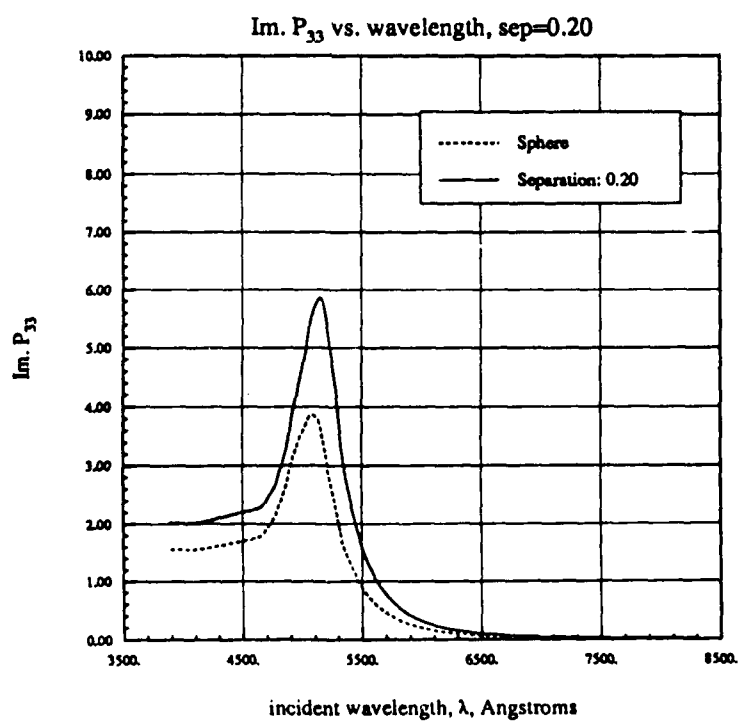


Figure 2.9 — Z-Incidence Absorption Spectrum, sep=0.2



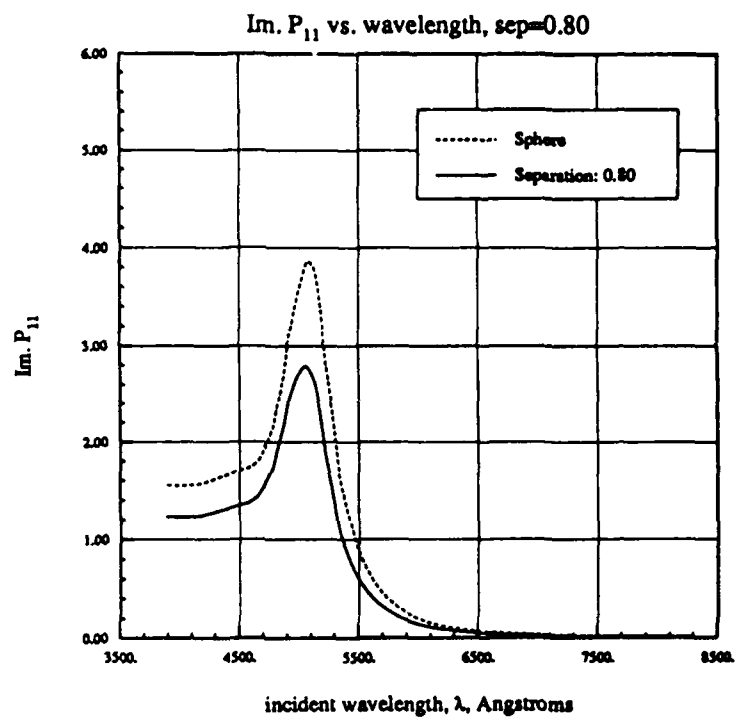


Figure 2.10 — X-Incidence Absorption Spectrum, sep=0.8

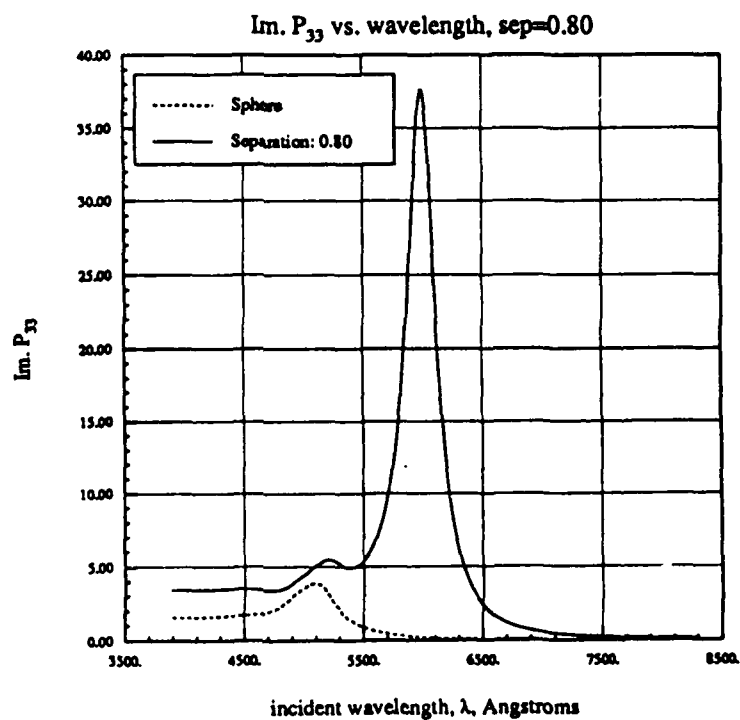


Figure 2.11 — Z-Incidence Absorption Spectrum, sep=0.8

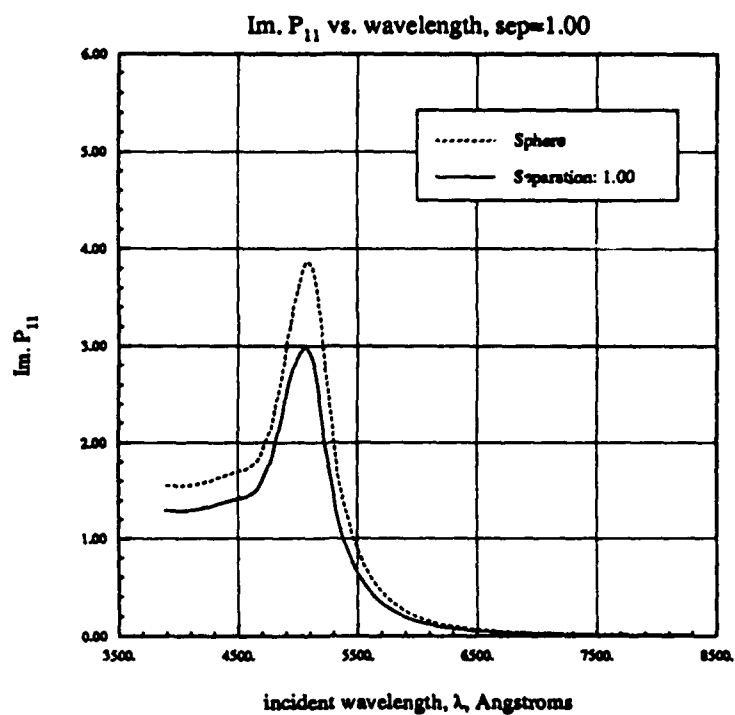


Figure 2.12 — X-Incidence Absorption Spectrum, sep=1.0

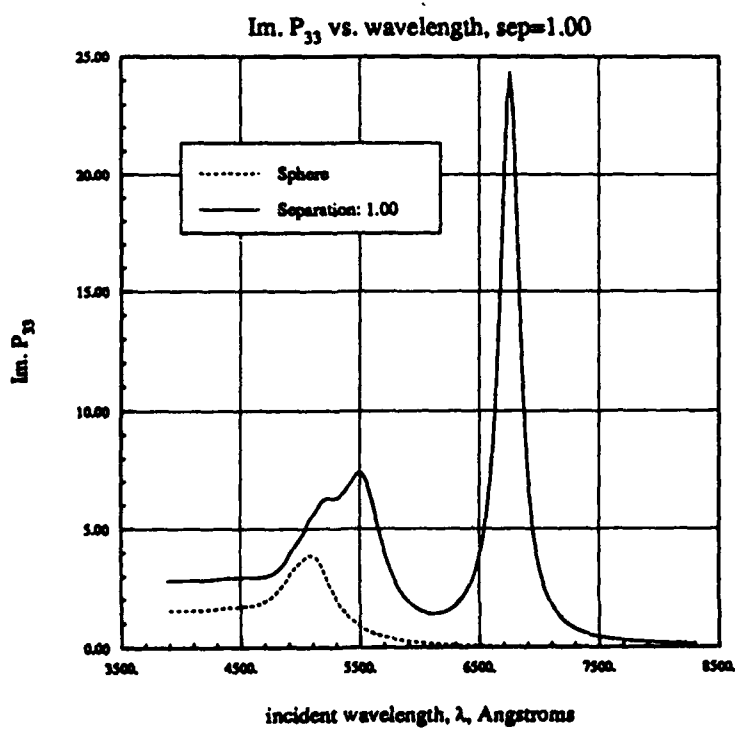


Figure 2.13 — Z-Incidence Absorption Spectrum, sep=1.0

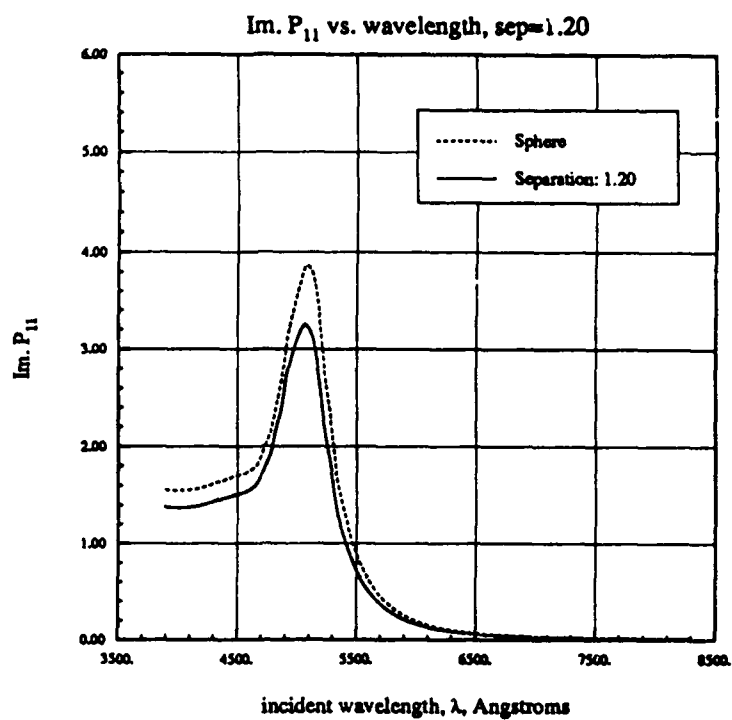


Figure 2.14 — X-Incidence Absorption Spectrum, sep=1.2

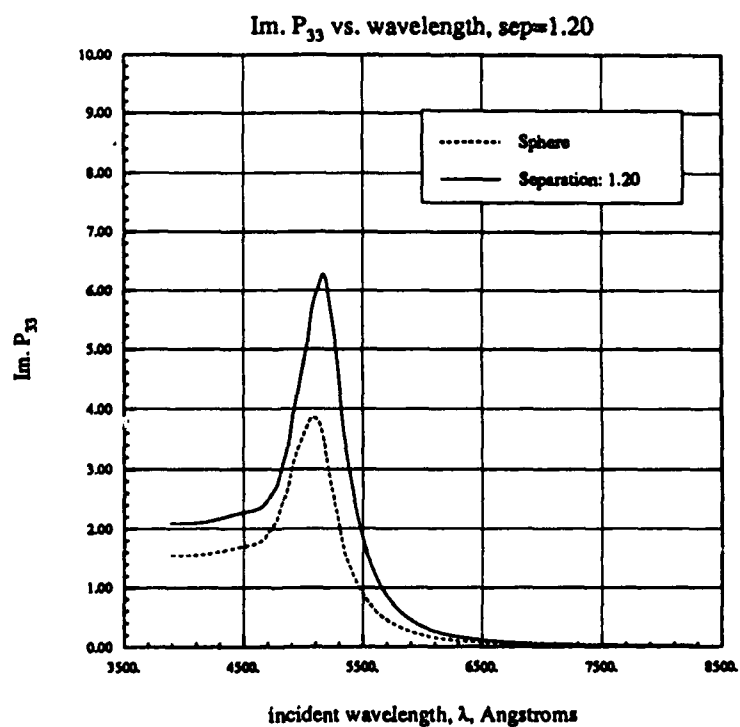


Figure 2.15 — Z-Incidence Absorption Spectrum, sep=1.2

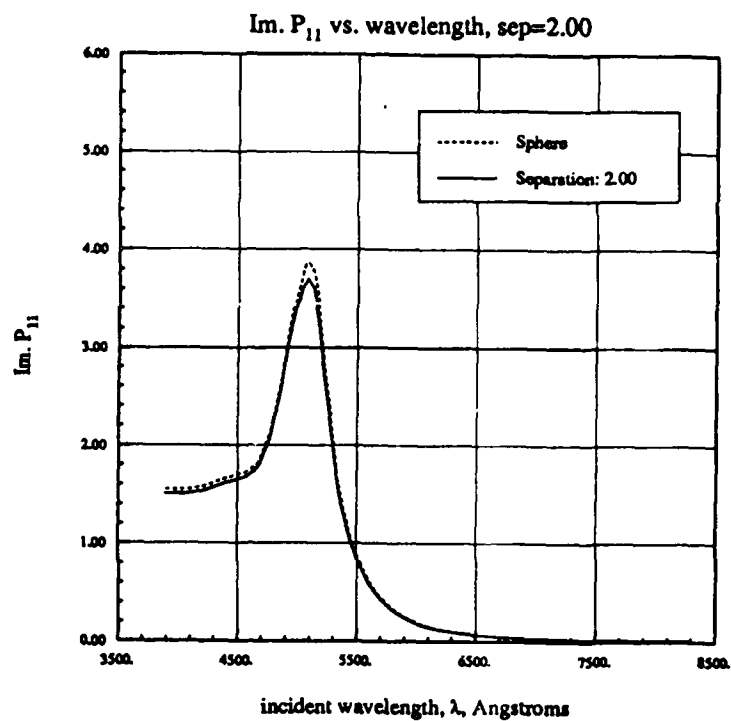


Figure 2.16 — X-Incidence Absorption Spectrum, sep=2.0

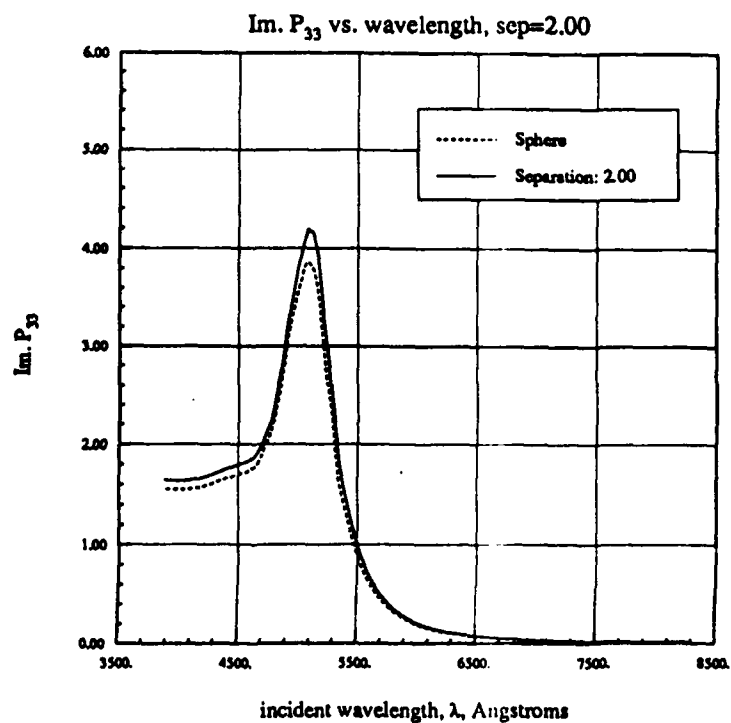


Figure 2.17 — Z-Incidence Absorption Spectrum, sep=2.0

The absorption cross-section plots are done for gold particles at approximately optical wavelengths. The most apparent similarity among these spectra is the only slight variability of the x-directed absorption: the single absorption peak is retained, with respect to its wavelength of occurrence, over the entire family of geometries. The magnitude of this absorption peak varies between 3 and 6 compared to the sphere's 4.

The variation of the z-directed spectra is greater, as one might expect from the previous field comparisons. The single-sphere peak appears to be retained, although it moves slightly (about 200 Angstroms) and its magnitude varies between 4 and 6. The most interesting feature, however, is the appearance of new absorption peaks. These peaks only occur for coagulated spheres that are nearly-whole spheres. In our examples, this is shown for separations of 0.8 and 1.0; ie. for nearly-whole, but coagulated spheres (0.8), and for whole but touching spheres (1.0). In each case the absorption peak is 6 to 10 times as strong as the single-sphere peak, and both are also shifted to longer wavelengths. The positions and strengths of these absorption peaks are highly dependent on geometry. Also of note, for the just-touching spheres case ( $\text{sep} = 1.0$ ) is a more complicated absorption spectrum in the region of the single-sphere peak: there appears to be two overlapping absorption peaks, each at a longer wavelength than the single-sphere peak.

The implications of these spectra for the colors of colloidal gold will be discussed later.

## IIa. Polarizability Tensors

The Polarizability Tensor elements are functions of complex  $\epsilon$ . Hence they are best displayed as surfaces in three-dimensional space. The following two figures (figs. 2.18 and 2.19) show a numerically-generated surface, and its fit, using the major resonances and their strengths.

A comparison of figures 2.18 and 2.19 shows that the fit (2.19), as far as it goes, does an excellent job. The error in regions not near  $\text{Re. } \epsilon_r = -1$  is on the order of 1%. This shows that in those regions the simple, intuitive, and physically meaningful model presented earlier is valid. In the region near  $\text{Re. } \epsilon_r = -1$ , however, the fit does not agree well with the numerically-generated data. The major reason for this is that the model chosen used only the three largest resonances. When the other, weaker, resonances are added to the model, the fit, of course, improves in that region. However, I personally am suspicious of the reality of these minor resonances and further work is planned to better understand them.

Absorption as a function of Complex Relative Permittivity ( $\epsilon_r$ ),  $\text{sep}=0.8$

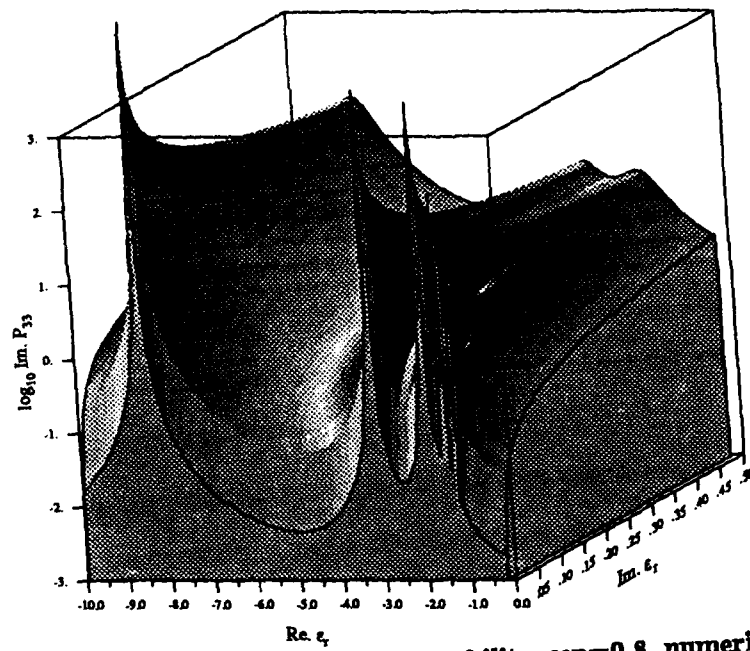


Figure 2.18 — Z-Incidence, Im. Polarizability,  $\text{sep}=0.8$ , numerical.

Absorption as a function of Complex Relative Permittivity ( $\epsilon_r$ ),  $\text{sep}=0.8$

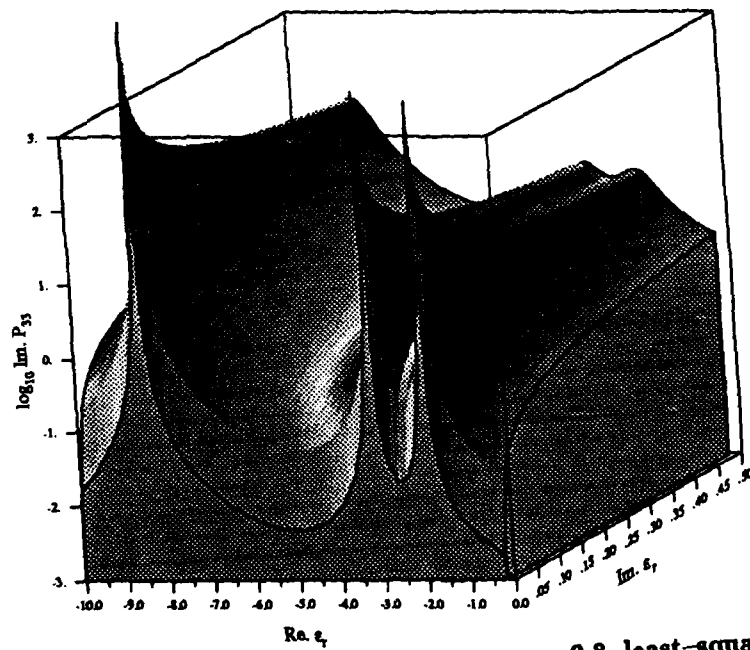


Figure 2.19 — Z-Incidence, Im. Polarizability,  $\text{sep}=0.8$ , least-squares fit.

## IIb. Resonances

As discussed in section one, the resonances, and associated strengths, of a particle completely determine the behavior of its Polarizability Tensor elements, as a function of relative permittivity. Hence, the resonances were investigated for the coagulated sphere family of shapes. Figures 2.20 and 2.21 show the behavior of the major resonances; major as determined by their strength. The strength was measured using the absorption cross-section of the particle with a dielectric constant equal to that of the resonant value with .1 added to it's imaginary part to give it some loss. The movement of these resonances in the  $\epsilon$ -plane can be seen as a cause for the variability in the color of a suspension of such particles when observed in white light: different particle shapes will cause the suspension to appear to have different colors than other shapes would.

These figures present the magnitude and position for the resonances observed in this family of geometries in a very complete way. The positions are clearly shown in fig. 2.20 for both x- and z-incidence (note the difference in the x-scales). The relative magnitudes of these resonances are displayed in fig. 2.21.

In these figures one can easily see the movement of the resonances away from that of the sphere ( $-2$ ), and their eventual return for the case of two separated spheres. Between these two extremes the behavior is quite different for the x- and z-directed cases: the x-directed resonance remains very close to  $\epsilon_r = -2$  and moves closer to  $\epsilon_r = \text{zero}$  during its deviation while the z-directed case spawns many resonances all increasing rapidly near separation = 1 (2 touching whole spheres). The major z-resonance is also much larger in magnitude than the x-resonance.

Please note that a previous paper (Weil, 1985) gave a plot similar to fig 2.20 here, but that the lines were drawn in the wrong direction due to insufficient data. That has been corrected here.



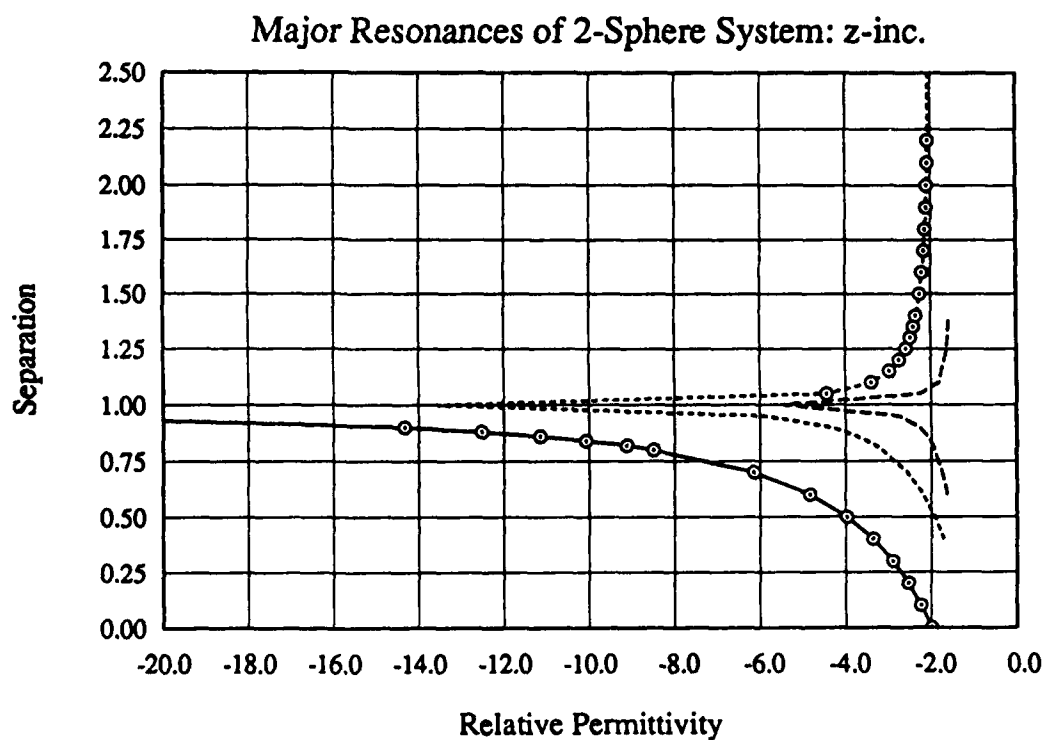
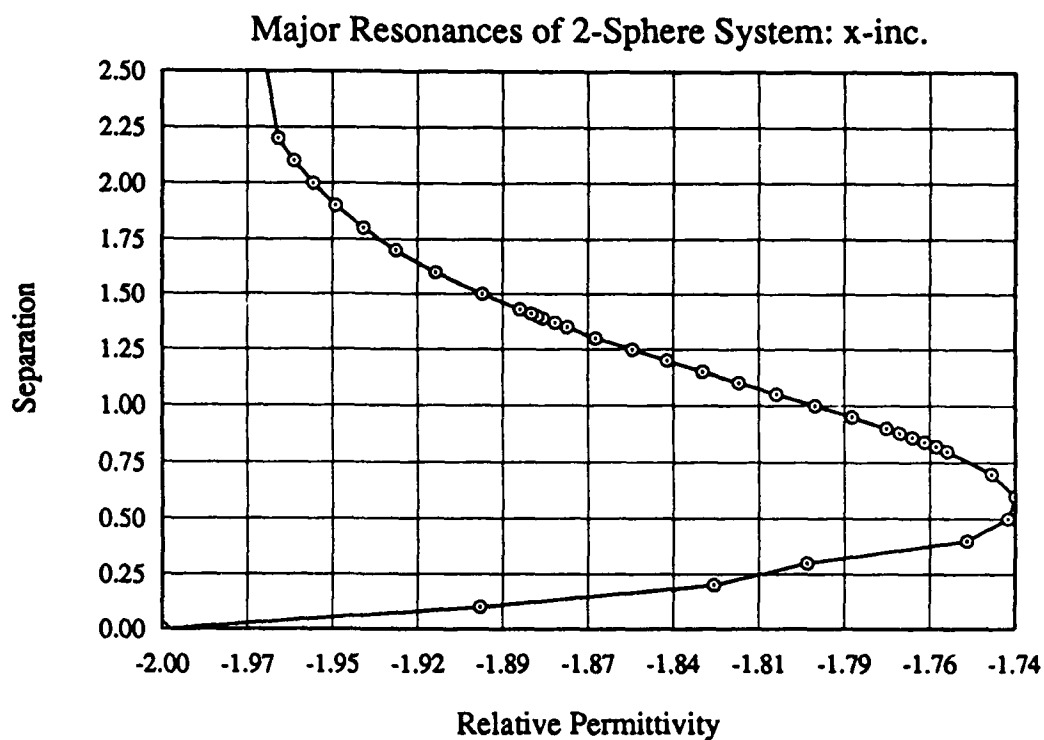


**Figure 2.20 — Major Resonances for Coagulated Spheres**

Resonance Strength as function of Geometry

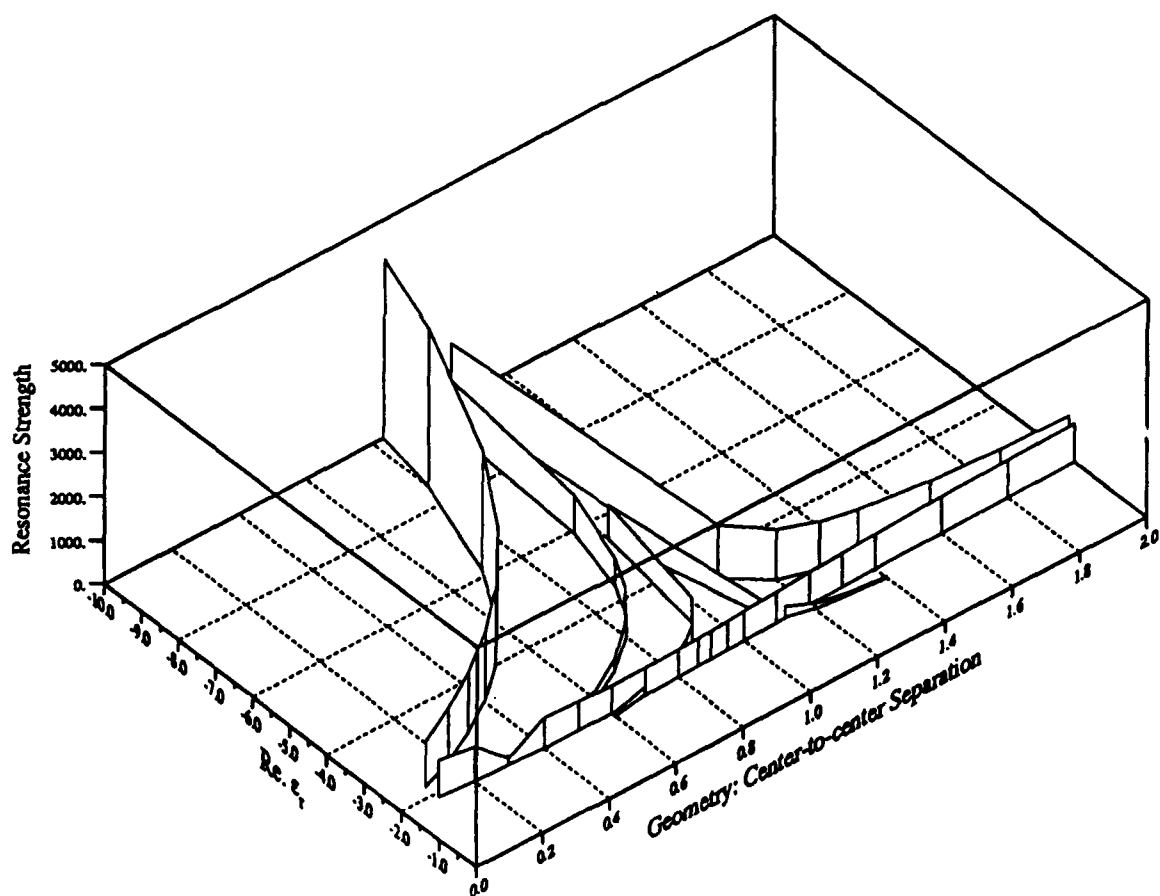


Figure 2.21 — Strengths of Major Resonances for Coagulated Spheres

A very intuitive method for understanding absorption spectra is to use the numerically-generated or modeled Polarizability Tensor elements and merely superimpose the plot of the relative permittivity on it. This gives a line on the wavy surface which can be visualized as a particular wavy slice through this surface to give rise to an absorption spectrum. This concept is shown in figures 2.22 and 2.23. Figure 2.22 shows the line on the surface of the Polarizability Tensor, while figure 2.23 shows the equivalent absorption cross-section, which in this case is the  $\text{Im.P}_{33}$ .

Looking at figure 2.22, note that the value of the bulk relative permittivity for gold at about 4000 Angstroms is about  $-2 + j6$ , and so the spectrum begins in the upper right corner. In comparing these two figures keep in mind that the surface is plotted with a logarithmic vertical scale, while the absorption spectrum uses a linear vertical scale. Despite this, we can still observe the two prominent absorption peaks in fig. 2.22. This is an intuitively pleasing way of thinking about absorption spectra for particular materials and particle shapes.

Absorption as a function of Complex Relative Permittivity ( $\epsilon_r$ ),  $\text{sep}=0.8$

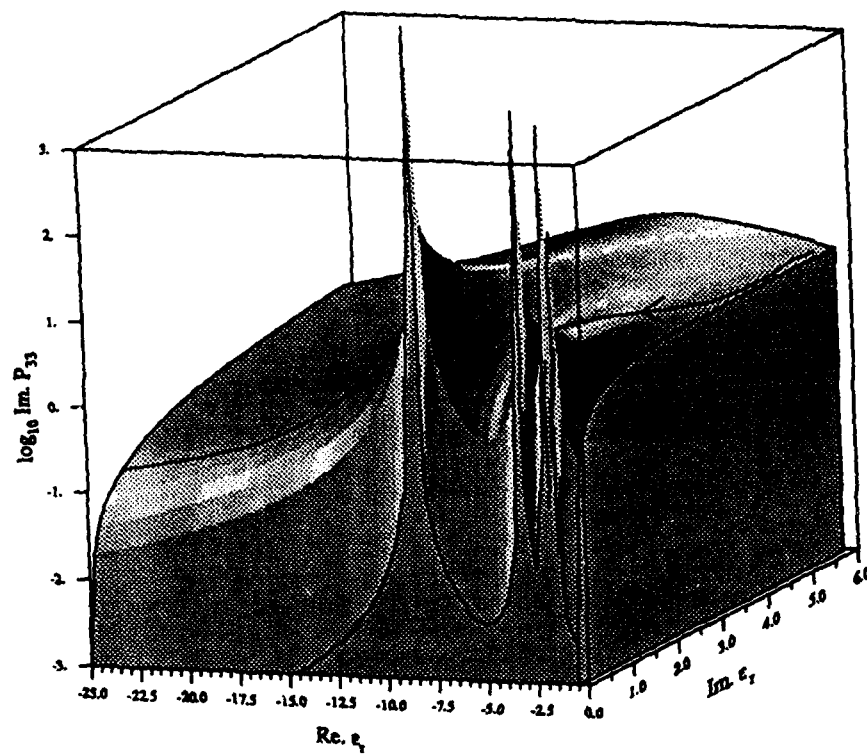


Figure 2.22 — Z-Incident, Im. Polarizability,  $\text{sep}=0.8$ , with  $\epsilon(\text{freq})$  for gold superimposed.

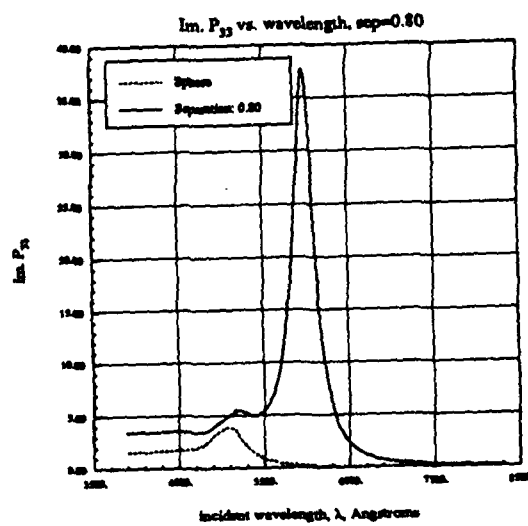
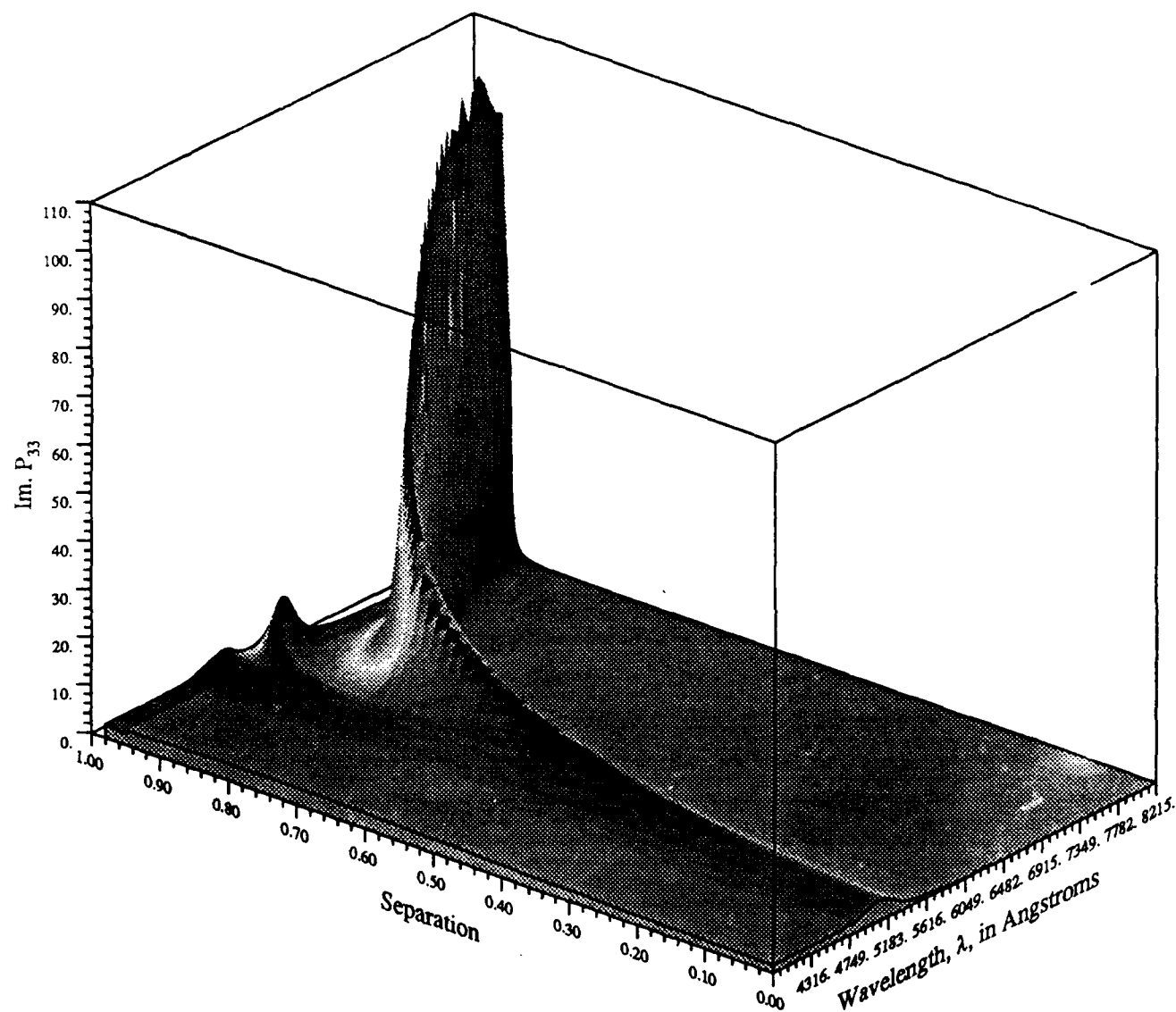


Figure 2.23 — Absorption Spectrum of Coagulated Gold Spheres,  $\text{sep}=0.8$ .

The model of the Polarizability Tensor elements can be used to generate a fit to the absorption cross-section as a function of geometry as well as wavelength. This scheme was used to generate figure 2.24, which is in fact a good fit to the available numerical data.

This figure shows the z-directed absorption spectrum for coagulated gold spheres as a function of separation. This data is a pretty good fit to the computer-generated numbers; we use a fit to generate this plot in order to save time. The features in this figure are the same as those noted for figures 2.9, 2.11, 2.13, 2.15, and 2.17: the z-directed absorption spectra. In this figure however, the continuous variation in the absorption peak's position and magnitude gives a better picture of their variability. As the separation increases toward 1 (from 0), and hence from a single sphere, through two coagulated spheres, and on to two just-touching spheres, we see that the single-sphere absorption peak "spawns" other peaks as the geometry becomes more concave. The first, and by far strongest, extra absorption peak begins to form at a separation of 0.4 or so. This peak then moves to progressively larger wavelengths, and increases in magnitude sharply after a separation of about 0.9, also spawned by the persistent single-sphere absorption peak. It moves toward longer wavelengths and increases slightly in magnitude by the time the two spheres are just touching.

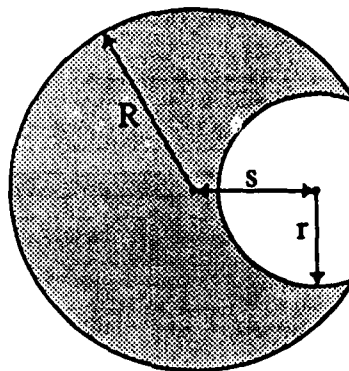
# Optical Absorption Spectrum of gold vs. Separation



**Figure 2.24 — Z-Incident Absorption Spectrum as function of Geometry.**

### III. SPHERE-WITH-CAVITY RESULTS

The geometry of this case is addressed in fig 3.1.



$R = 0.5$  -- radius of solid sphere  
 $s$  = center-to-center separation  
 $r$  = radius of spherical hole

#### EXAMPLES

$s=0.0, r=0.3$  -- a hollow spherical shell: ☉  
 $s=0.2, r=0.2$  -- off-center spherical hole inside sphere: ☉  
 $s=0.3, r=0.4$  -- a spherical bite out of side of sphere: ☹

Figure 3.1 — The Sphere-with-Cavity Geometry

The fields were plotted with a variety of separations and also at many different frequencies; each different frequency corresponds to a different  $\epsilon$  for gold, tabulated in Physik Daten [ 1981 ]. Due to symmetry, only a portion of the field structure is shown. That part of the field that intersects the plane through the symmetry axis (see fig 3.2) and is in the first two quadrants (darkened piece of the plane) is displayed in the field plots. The wire mesh is meant to represent the surface of the (see-thru) particle that is being halved by the cutting plane.

Typical field plots are shown in figs 3.3–3.8 for the three typical geometries, and an arbitrary relative permittivity. Each of the field plots has the real part and imaginary part of the potential for a particular shape, frequency and ' incident ' E-field direction:

x-directed means E is vertical at infinity.

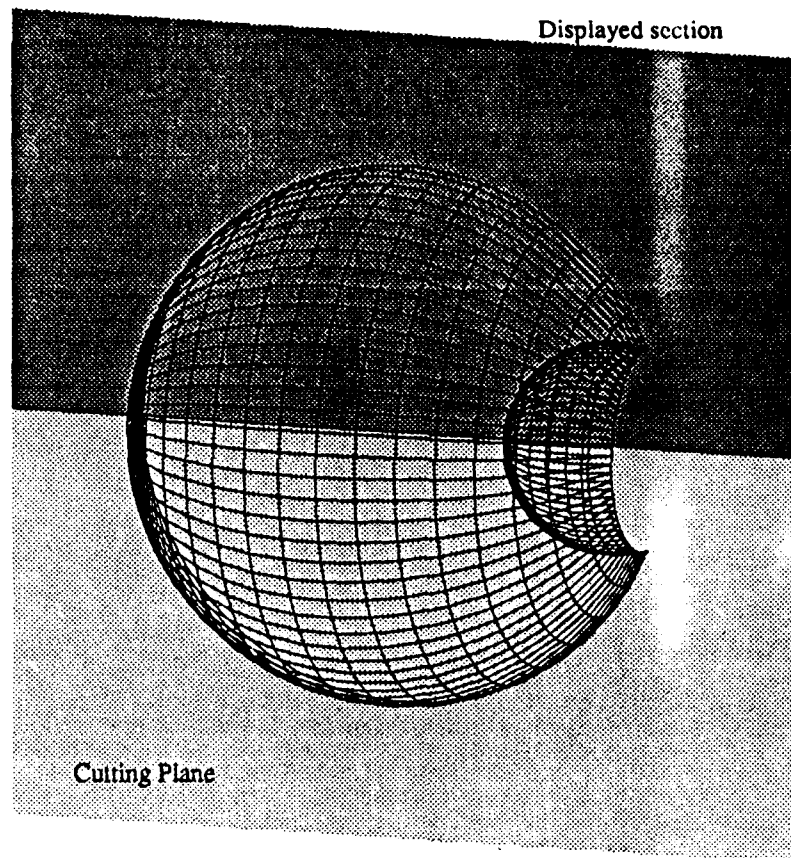


Figure 3.2 — Position of Field Plots in relation to the particle

$z$ -directed means  $E$  is horizontal at infinity.

Each plot has 4–6 equipotential lines, while  $\Delta V$  (or “spacing in volts” on the plots) between them varies from plot-to-plot. Hence a large value for  $\Delta V$  means that we have high local  $E$ -field concentrations.

$\tau$  in each plot is the value for the relative dielectric constant.

The dimensionless average absorption cross-section, as described earlier, was plotted for each geometry as a function of free-space wavelength. Typical spectra for each of the three typical geometries previously used are shown in figs 3.9–3.13.



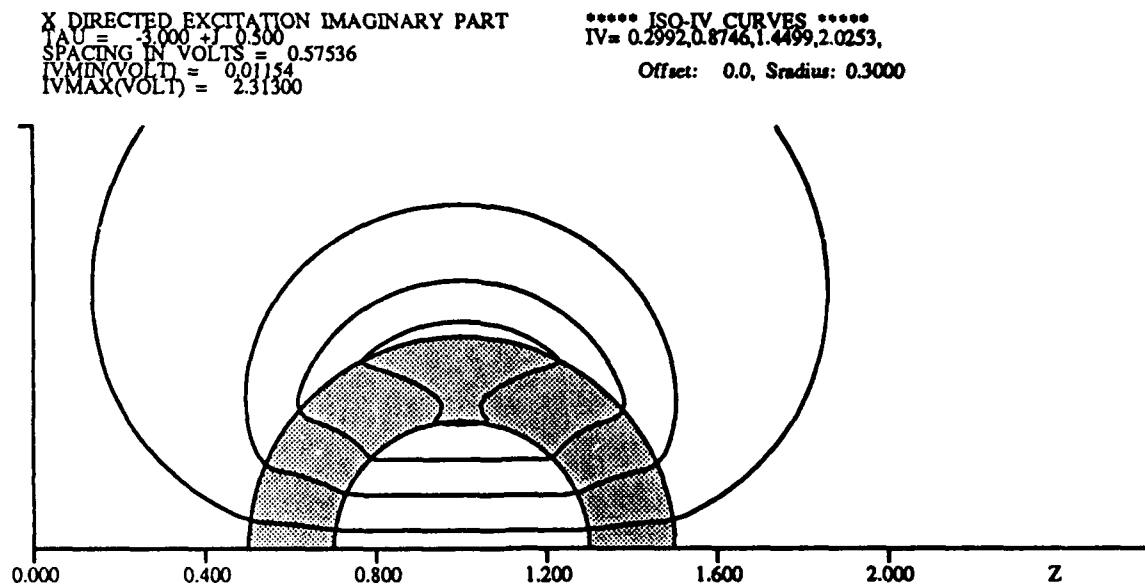
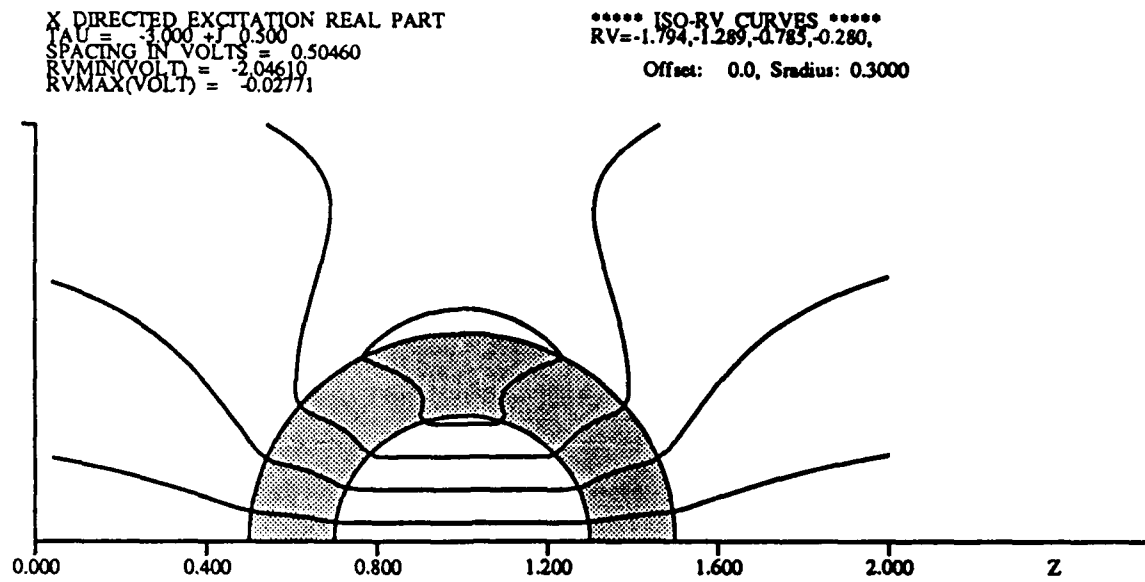
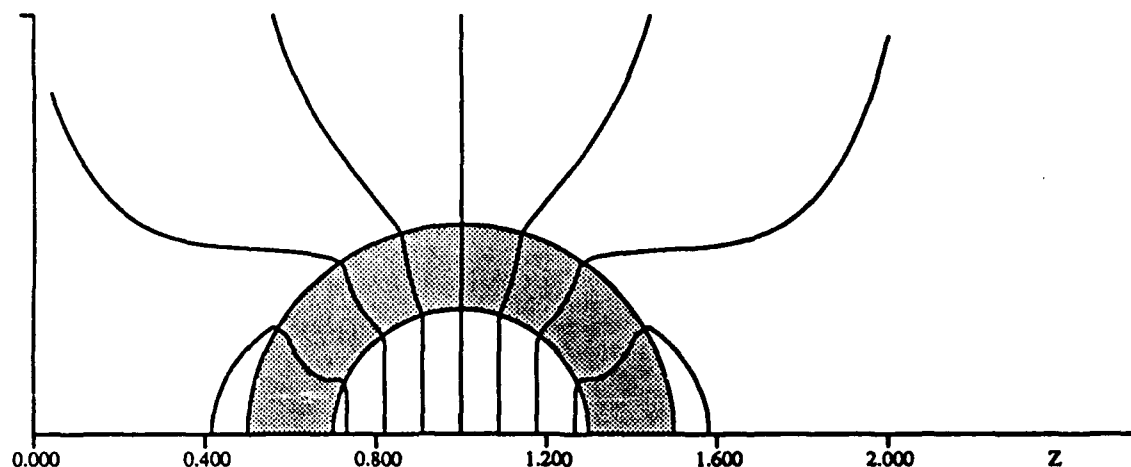


Figure 3.3 — X-Incident Equi-Potential lines for a Hollow Shell.

Z DIRECTED EXCITATION REAL PART  
 $\tau = -3.000 + j 0.500$   
 SPACING IN VOLTS = 0.57306  
 $R_{V\min}(\text{VOLT}) = -3.00628$   
 $R_{V\max}(\text{VOLT}) = 1.00514$

\*\*\*\*\* ISO-RV CURVES \*\*\*\*\*  
 $R_V = -2.720, -2.147, -1.574, -1.001, -0.428,$   
 $0.1435, 0.7186,$   
 Offset: 0.0, Sradius: 0.3000



Z DIRECTED EXCITATION IMAGINARY PART  
 $\tau = -3.000 + j 0.500$   
 SPACING IN VOLTS = 0.64668  
 $I_{V\min}(\text{VOLT}) = -2.26324$   
 $I_{V\max}(\text{VOLT}) = 2.26353$

\*\*\*\*\* ISO-IV CURVES \*\*\*\*\*  
 $I_V = -1.940, -1.293, -0.647, 0.00014, 0.6468,$   
 $1.2935, 1.9402,$   
 Offset: 0.0, Sradius: 0.3000

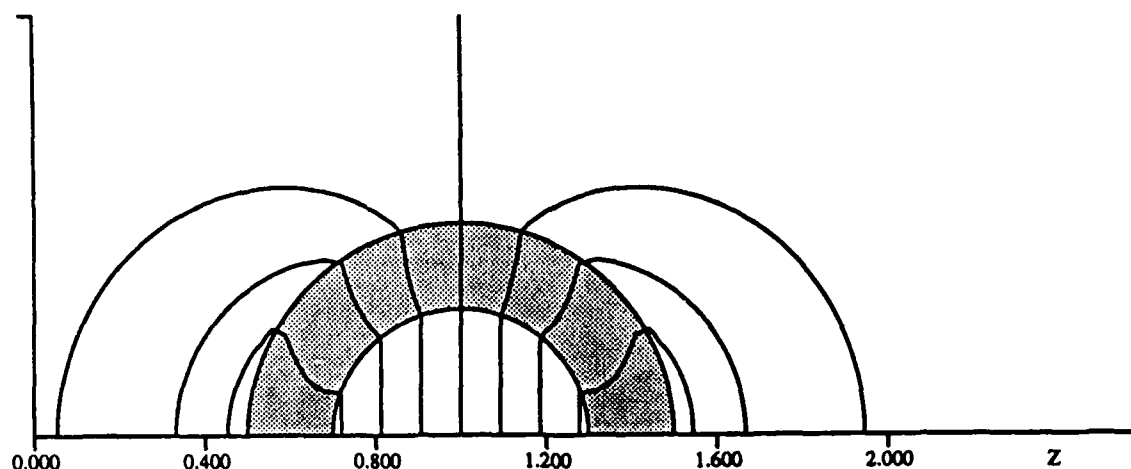


Figure 3.4 — Z-Incident Equi-Potential lines for a Hollow Shell.

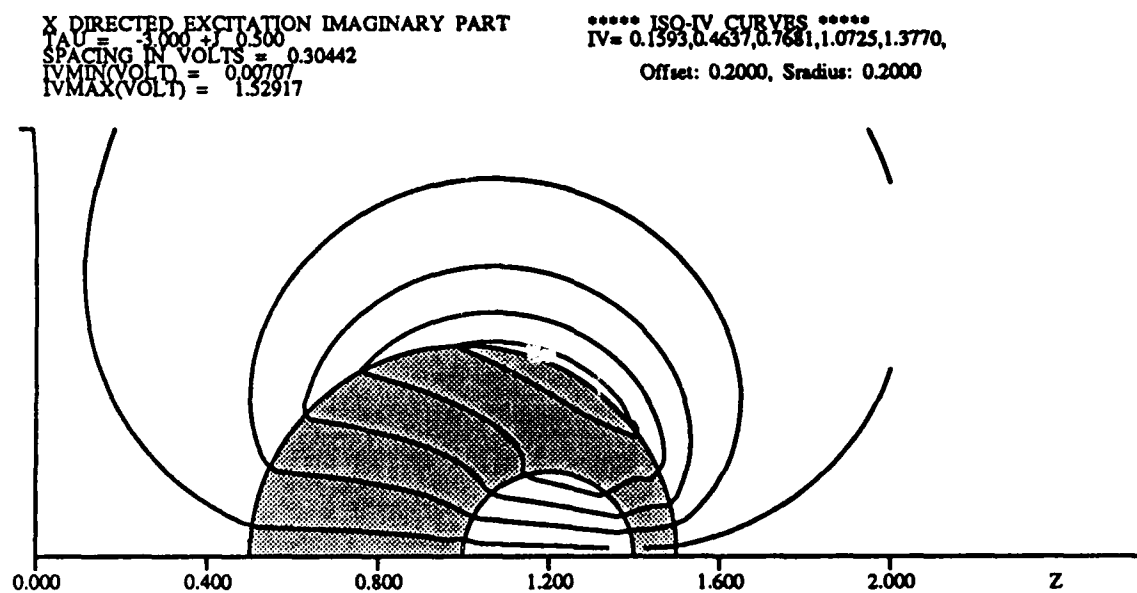
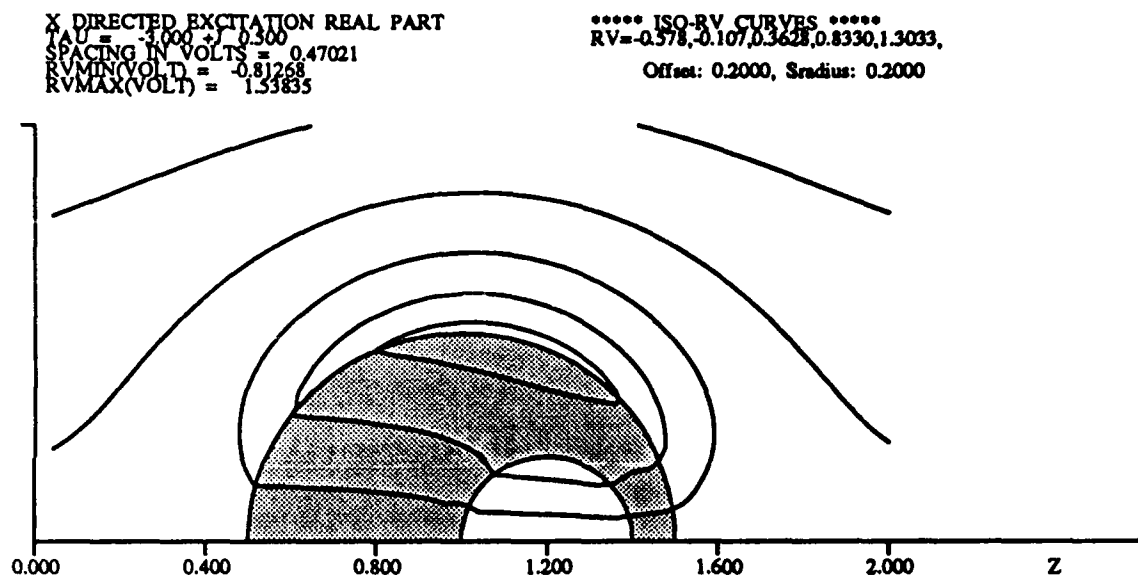


Figure 3.5 — X-Incident Equi-Potential lines for an Off-center Hole.

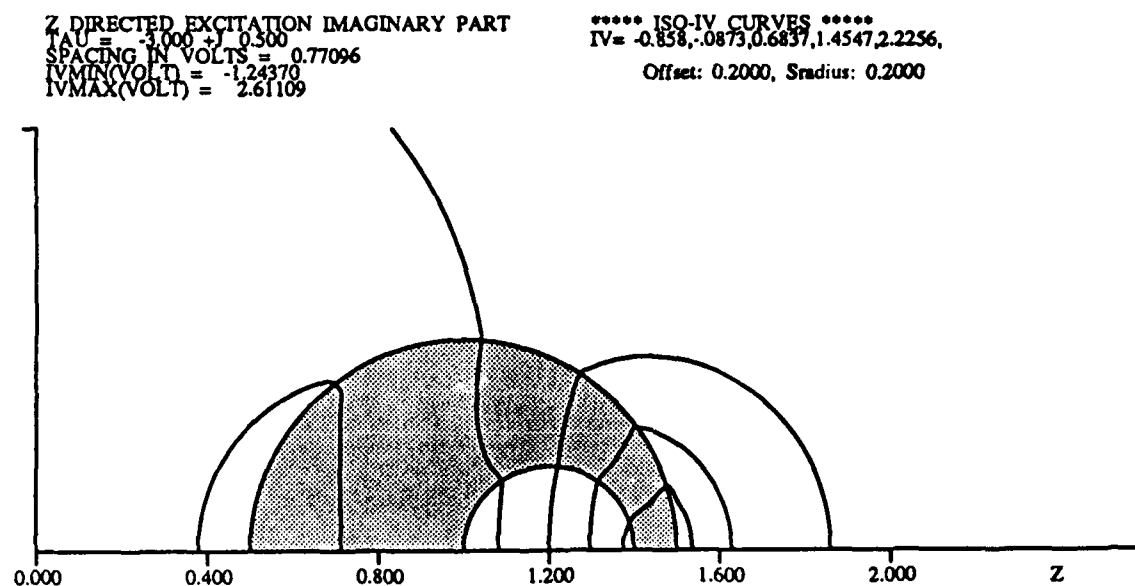
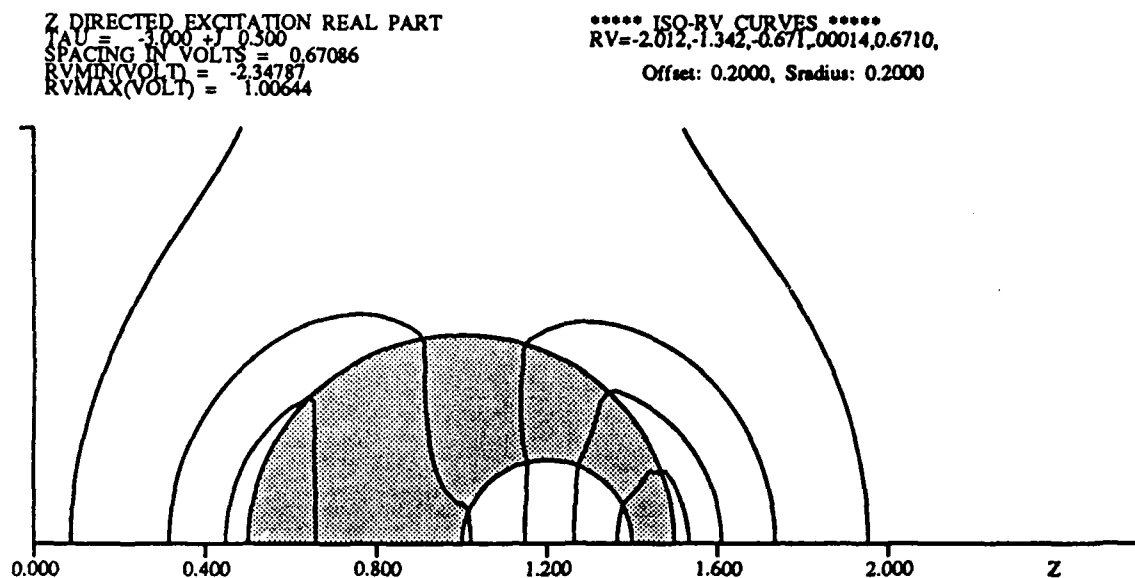
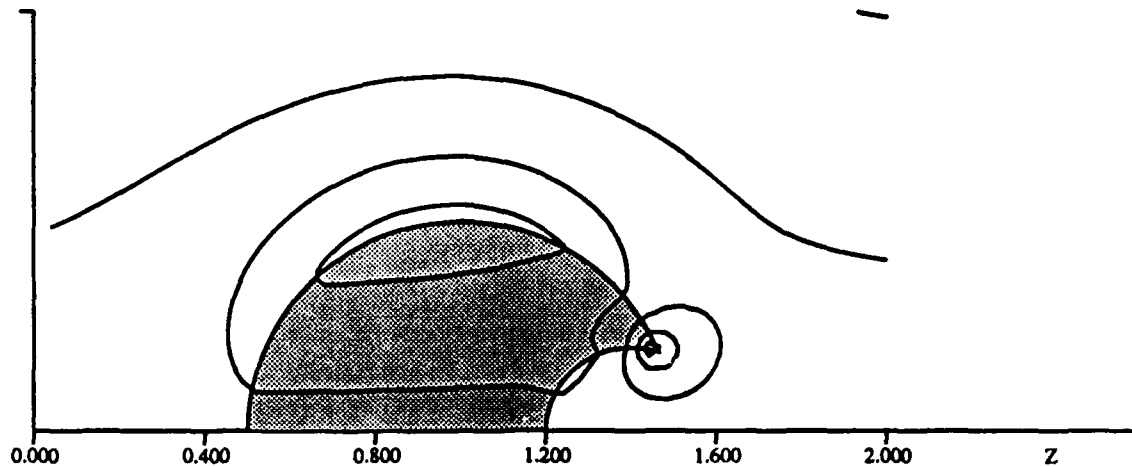


Figure 3.6 — Z-Incident Equi-Potential lines for an Off-center Hole.

X DIRECTED EXCITATION REAL PART  
 $\tau = -3.000 + j 0.300$   
 SPACING IN VOLTS = 0.54172  
 $V_{MIN}(VOLT) = -1.69187$   
 $V_{MAX}(VOLT) = 1.01672$

\*\*\*\*\* ISO-RV CURVES \*\*\*\*\*  
 $RV = -1.421, -0.879, -0.338, 0.2041, 0.7459,$   
 Offset: 0.4000, Sradius: 0.2000



X DIRECTED EXCITATION IMAGINARY PART  
 $\tau = -3.000 + j 0.300$   
 SPACING IN VOLTS = 0.17067  
 $V_{MIN}(VOLT) = 0.00419$   
 $V_{MAX}(VOLT) = 0.85753$

\*\*\*\*\* ISO-IV CURVES \*\*\*\*\*  
 $IV = .08952, 0.2602, 0.4309, 0.6015, 0.7722,$   
 Offset: 0.4000, Sradius: 0.2000

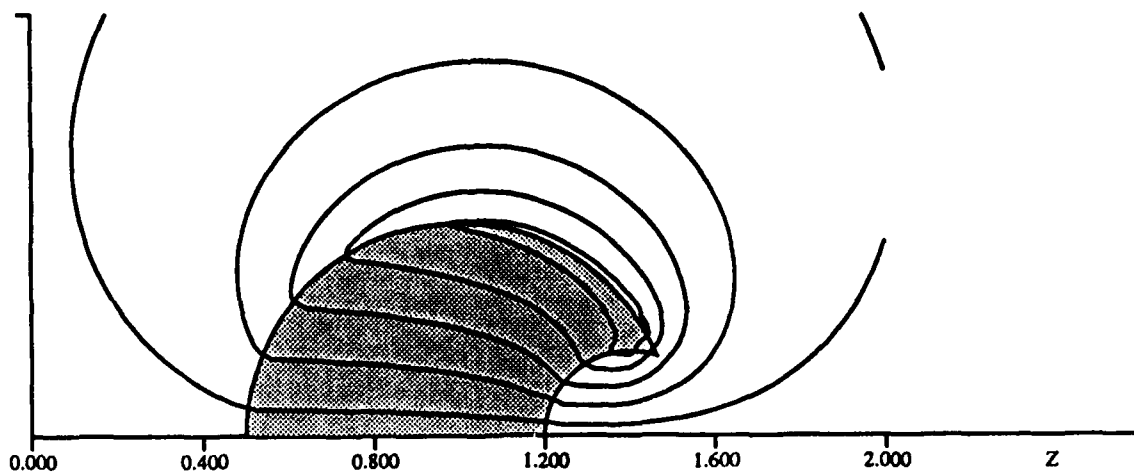
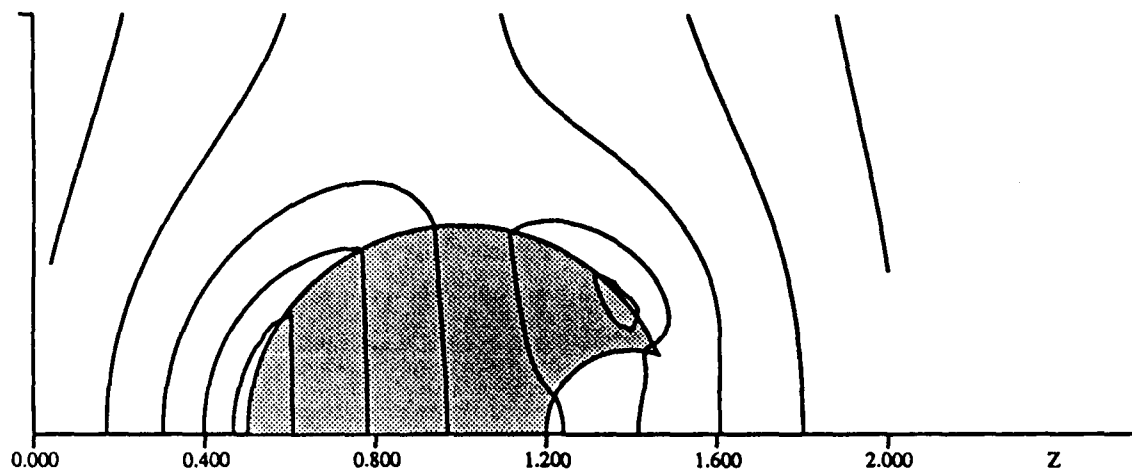


Figure 3.7 — X-Incident Equi-Potential lines for a Spherical Aperture in a Sphere.

Z DIRECTED EXCITATION REAL PART  
 $\tau = 1.000 + j 0.300$   
 SPACING IN VOLTS = 0.35412  
 $V_{\min}(\text{VOLT}) = -1.93479$   
 $V_{\max}(\text{VOLT}) = -0.16420$

\*\*\*\*\* ISO-RV CURVES \*\*\*\*\*  
 $RV = -1.758, -1.404, -1.049, -0.695, -0.341,$   
 Offset: 0.4000, Sradius: 0.2000



Z DIRECTED EXCITATION IMAGINARY PART  
 $\tau = 1.000 + j 0.300$   
 SPACING IN VOLTS = 0.73221  
 $V_{\min}(\text{VOLT}) = -0.92716$   
 $V_{\max}(\text{VOLT}) = 2.73389$

\*\*\*\*\* ISO-IV CURVES \*\*\*\*\*  
 $IV = -0.561, 0.1712, 0.9034, 1.6356, 2.3678,$   
 Offset: 0.4000, Sradius: 0.2000

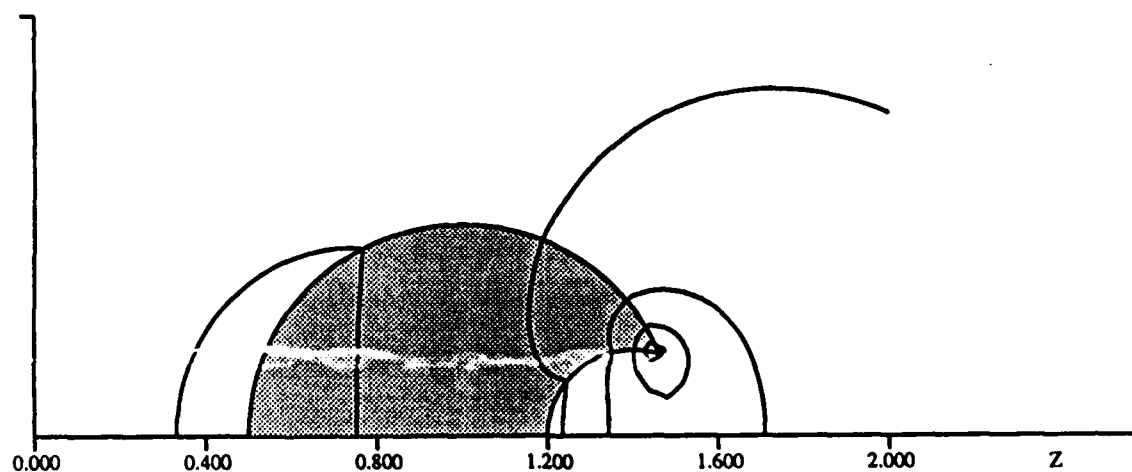


Figure 3.8 — Z-Incident Equi-Potential lines for a Spherical Aperture in a Sphere.

The typical field plots shown in the preceding figures (3.3–3.8) are meant to show the different geometries and typical field lines. All are for  $\epsilon_r = -3. + j0.5$ . No detailed study has yet been made of resonant field structures as was done for the coagulated spheres. Some features that one would intuitively expect are apparent: the spherical shell has a uniform field inside the hole and has x-directed and z-directed fields that are the same but for a rotation; the non-symmetric shapes show the general tendency to have larger field strengths in their regions of highest structural variability. Specifically, the off-center hole geometry has a higher field in the thinner part of the shell, and the sphere with the surface hole has a large concentration near the cusp caused by this hole.

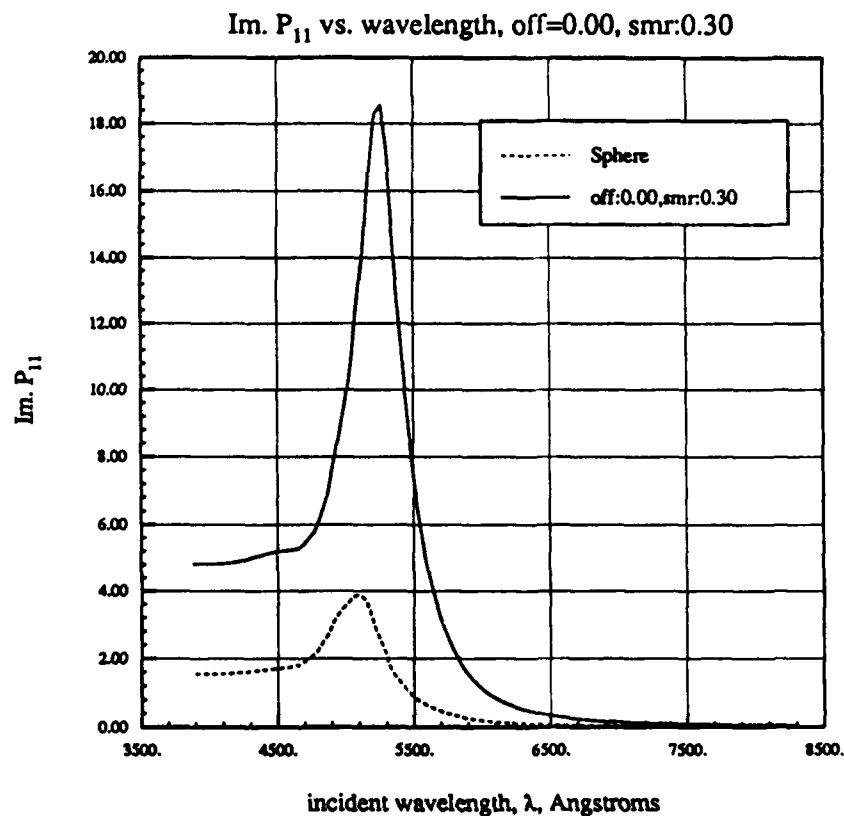


Figure 3.9 — Absorption Spectrum for a Hollow Shell.

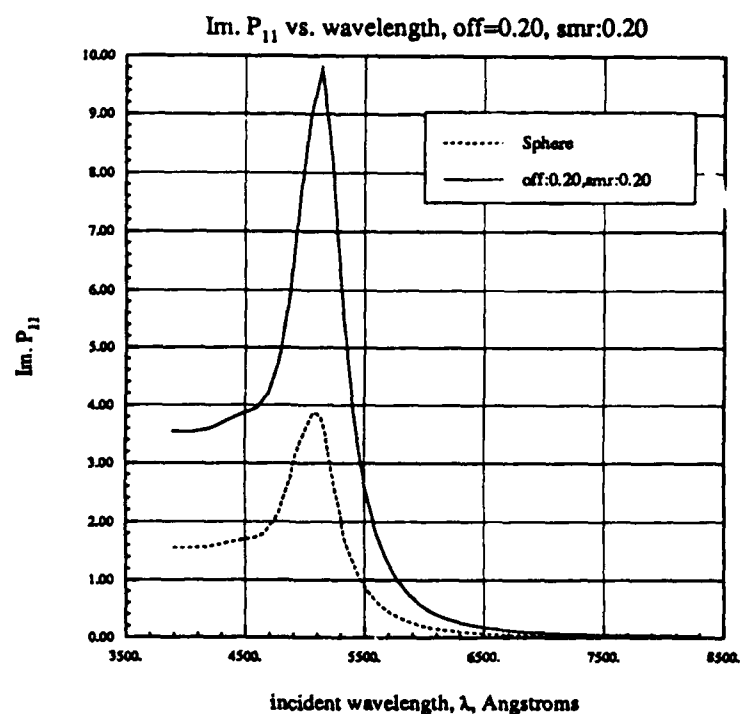


Figure 3.10 — X-Incident Absorption Spectrum for an Off-center Hole.

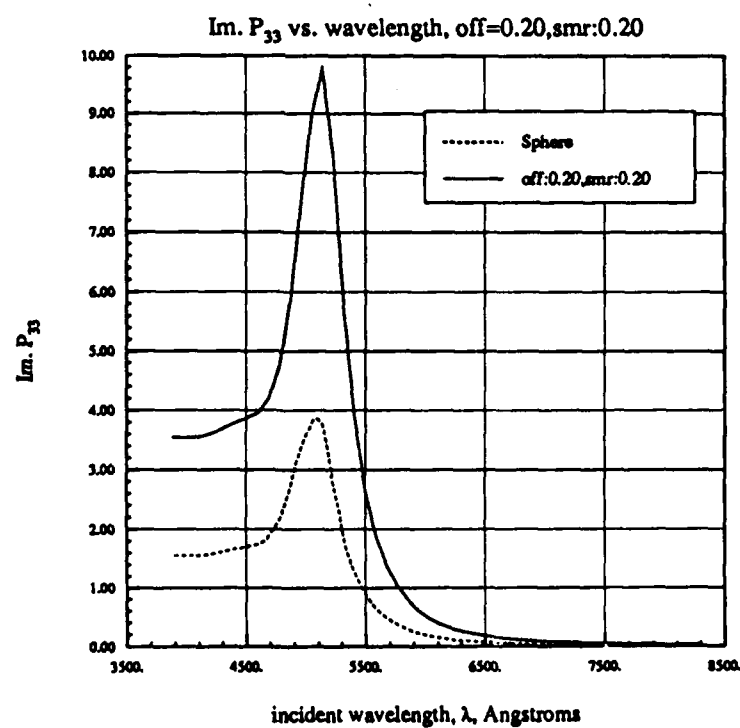


Figure 3.11 — Z-Incident Absorption Spectrum for an Off-center Hole.



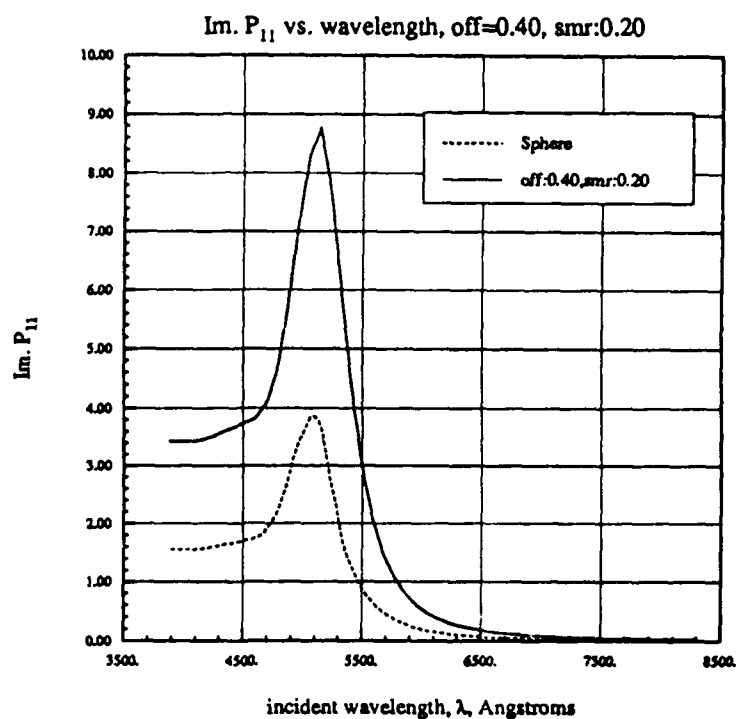


Figure 3.12 — X-Incident Absorption Spectrum for a Spherical Aperture in a Sphere.

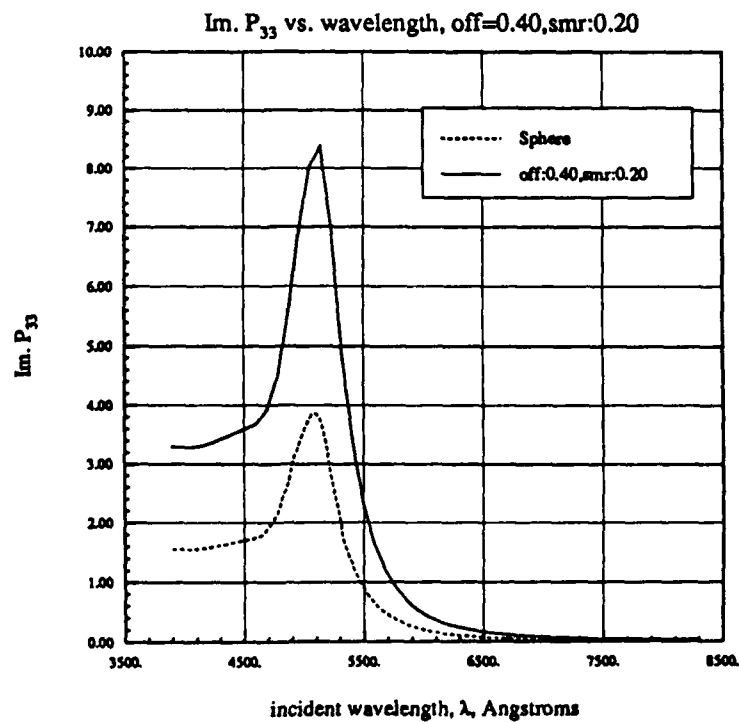


Figure 3.13 — Z-Incident Absorption Spectrum for a Spherical Aperture in a Sphere.

Some typical absorption spectra for gold particles are shown in figs 3.9-3.13. The spectra are remarkably similar. In each case the one absorption peak occurs at nearly the same wavelength as for a single sphere. Also, in each case the absorption magnitude is 2.5 to 5 times that of a single sphere. Lastly, the difference between x- and z-directed absorption was very small, almost non-existent, amounting to a small change in absorption magnitude. These results are surprising in light of the extreme differences seen for different geometries and incidence directions for the coagulated spheres in the previous section.

## IIa. Polarizability Tensors

The Polarizability Tensor elements are functions of complex  $\epsilon$ . Hence they are best displayed as surfaces in three-dimensional space. Specifically the  $\text{Im.}P_{33}$  is shown for each of the three typical shapes in figures 3.14 through 3.16

These three surfaces point up to us why the absorption spectra are similar. Each surface shows complicated resonance behavior for  $\text{Re. } \epsilon_r \in (0, -4)$  but are uniformly decaying outside that range. (Note: the surfaces for  $\text{Im. } P_{11}$  are similarly complicated and clustered between 0 and  $-4$ .) When the imaginary part of  $\epsilon_r$  gets larger than about 0.4 the surfaces are similar and difficult to distinguish. Hence for a permittivity trace in the  $\epsilon_r$ -plane that doesn't enter this region, or which only goes through slightly, the spectra will be difficult to distinguish. That is what happened in the previous plots. Also note that the hollow spherical appears to have the same resonance as the single sphere, except shifted, and to have another small resonance near zero. The other two geometries have very similar, but complex, surfaces. Further work in this area, especially modeling, is continuing.

Absorption as a function of Complex Relative Permittivity ( $\epsilon_r$ ), off=.0, smr=.3

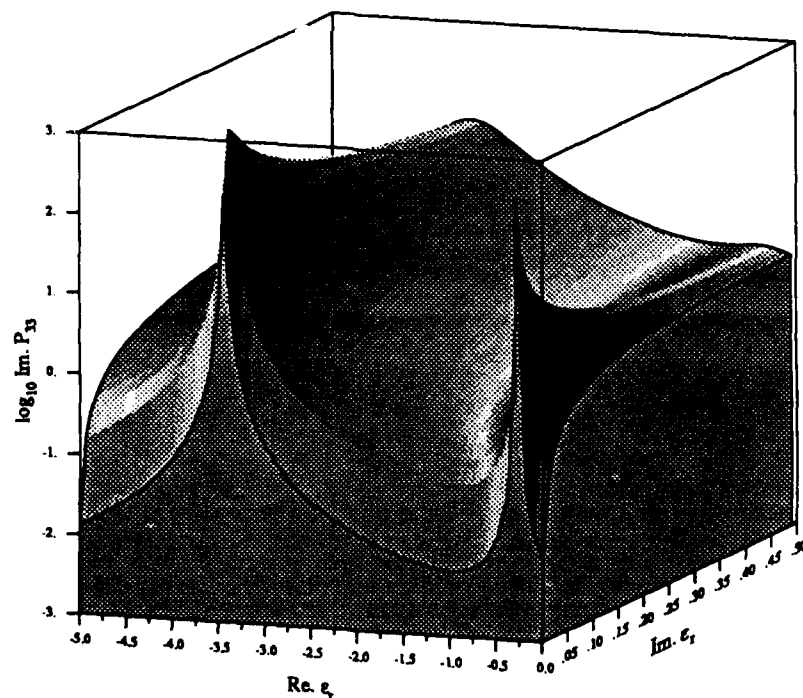


Figure 3.14 —  $\text{Im.}$  Polarizability for a Spherical Shell.

Absorption as a function of Complex Relative Permittivity ( $\epsilon_r$ ), off=.2, smr=.2

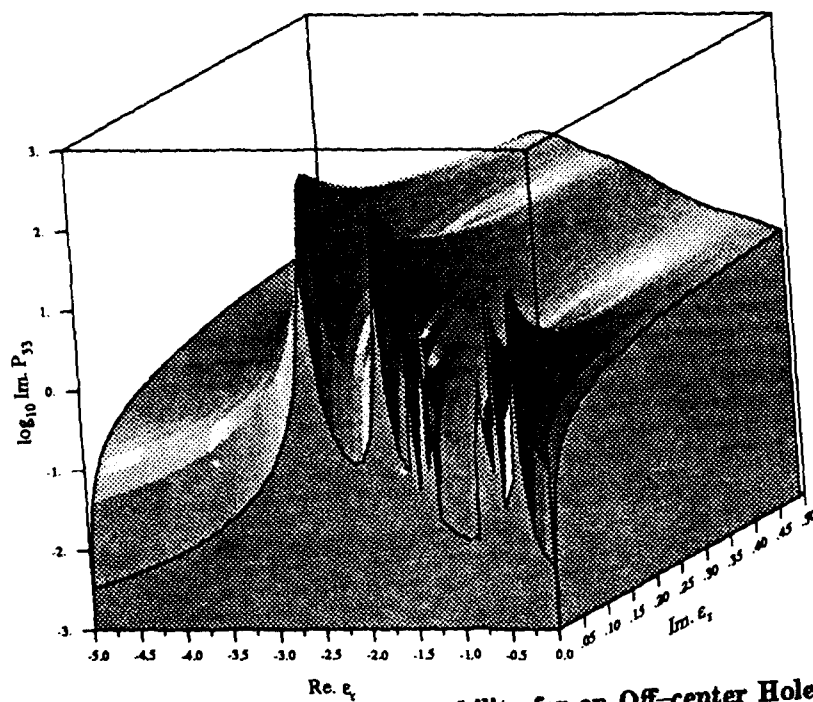


Figure 3.15 — Im. Polarizability for an Off-center Hole.

Absorption as a function of Complex Relative Permittivity ( $\epsilon_r$ ), off=.4, smr=.2

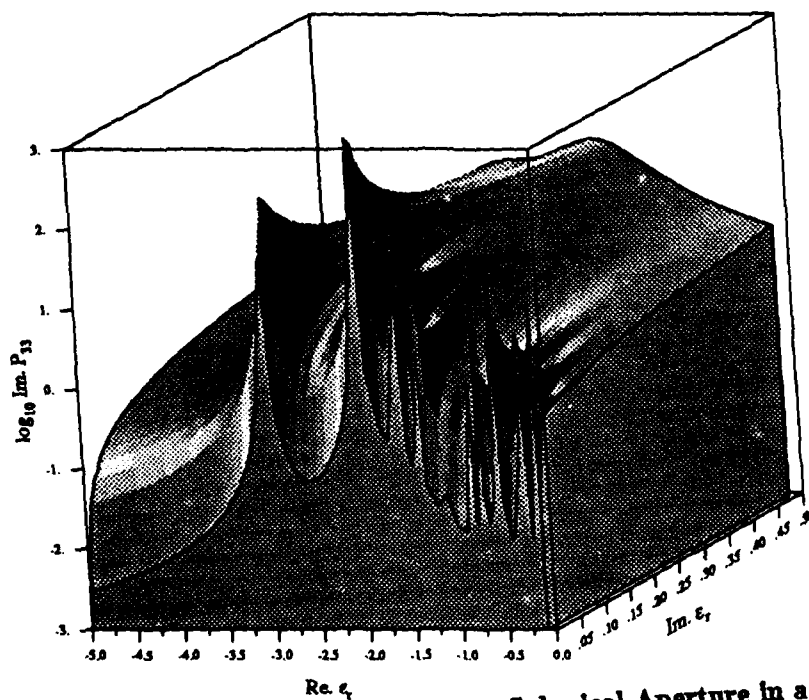


Figure 3.16 — Im. Polarizability for a Spherical Aperture in a Sphere.

### IIIb. Resonances

As discussed in section one, the resonances, and associated strengths, of a particle completely determine the behavior of its Polarizability Tensor elements, as a function of relative permittivity. Hence, the resonances were investigated for the three typical cavity shape families. Figures 3.17, 3.18, and 3.19 show the behavior of the major resonances; major as determined by their strength. The movement of these resonances in the cause for the variability in the color of a suspension of such particles when observed in white light: different particle shapes will appear to have different colors than others.

Further insight into the absorption spectra of this family of shapes can be gleaned from these figures. They show the positions of the major resonances of each of the three canonical shapes. The resonances of the hollow spherical shell are shown in fig. 3.17. They follow the familiar track, starting near  $-2$  and diverging to  $-\infty$  as the shell gets thinner. The other cases were quite different. The off-center hole family (position of hole was varied) had a major resonance near  $-2$  and stayed there, for both x- and z-incidence. The hole-in-surface family varied the hole size, and for x-incidence the resonance stayed relatively near  $-2$ , although it began to diverge as the hole size increased. For z-incidence the resonance diverged more rapidly, but for both x- and z-incidences the resonances diverged very slowly in comparison to those for the hollow sphere or for the coagulated sphere.

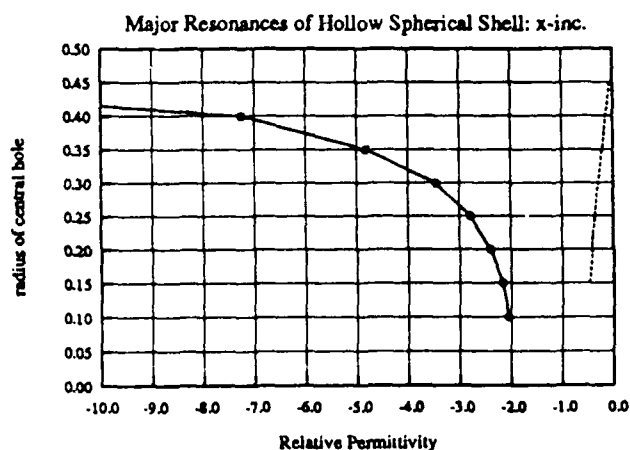
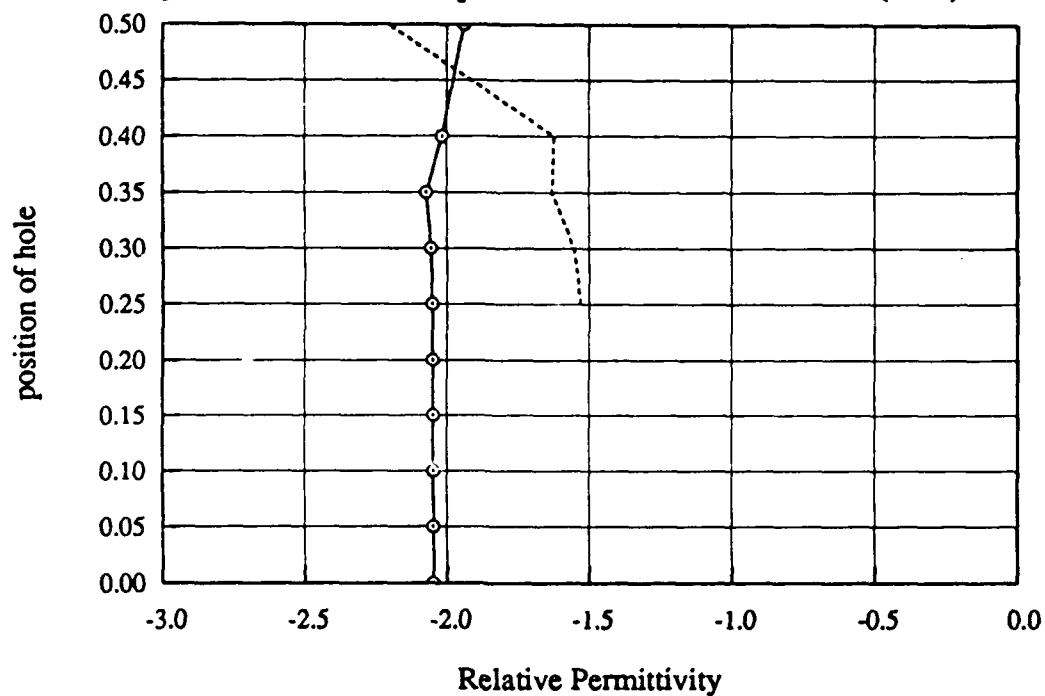


Figure 3.17 — Major Resonances of Spherical Shell as function of Hole Radius.

Major Resonances of Sphere with Off-Center Hole ( $r=.1$ ): x-inc.



Major Resonances of Sphere with Off-Center Hole ( $r=.1$ ): z-inc.

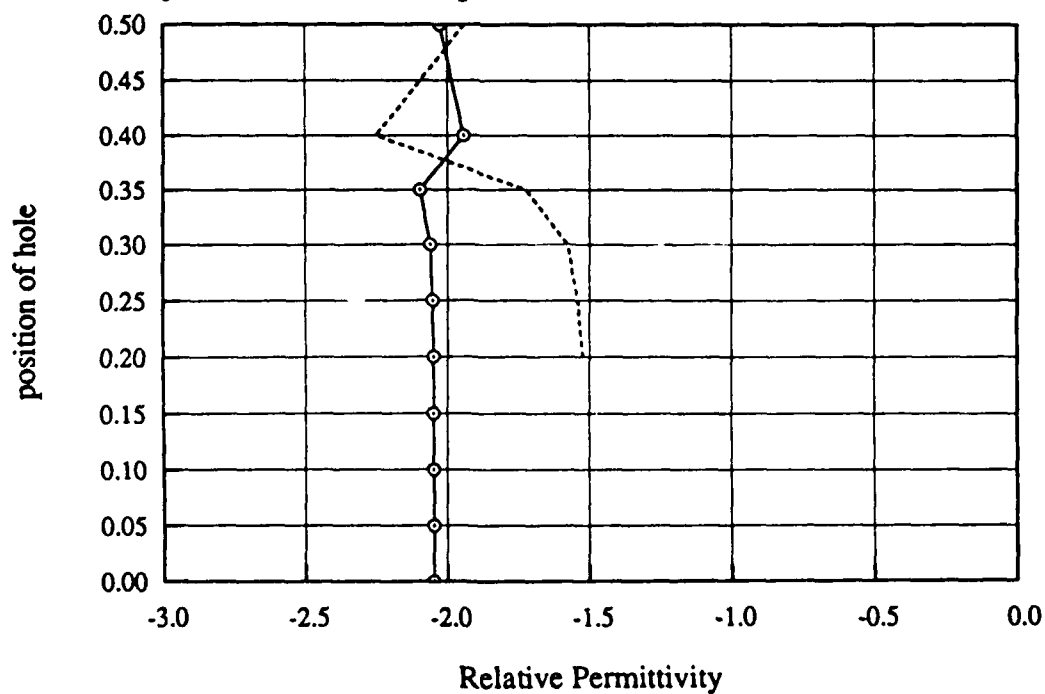


Figure 3.18 — Major Resonances of Off-center Hole as function of Hole Position.

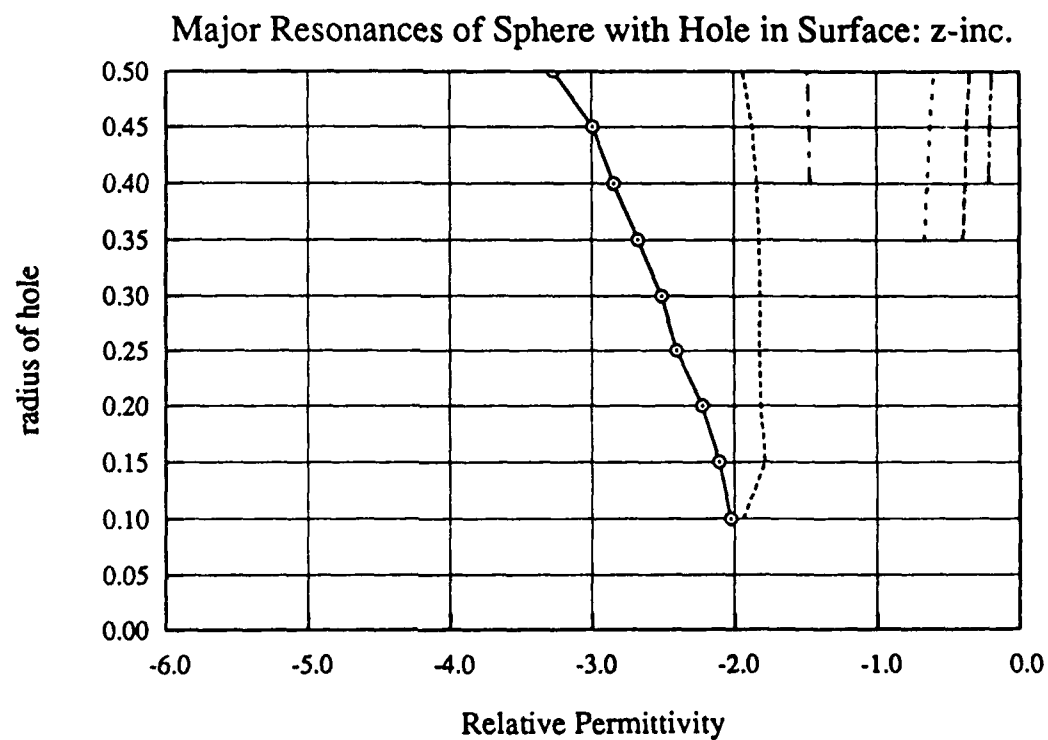
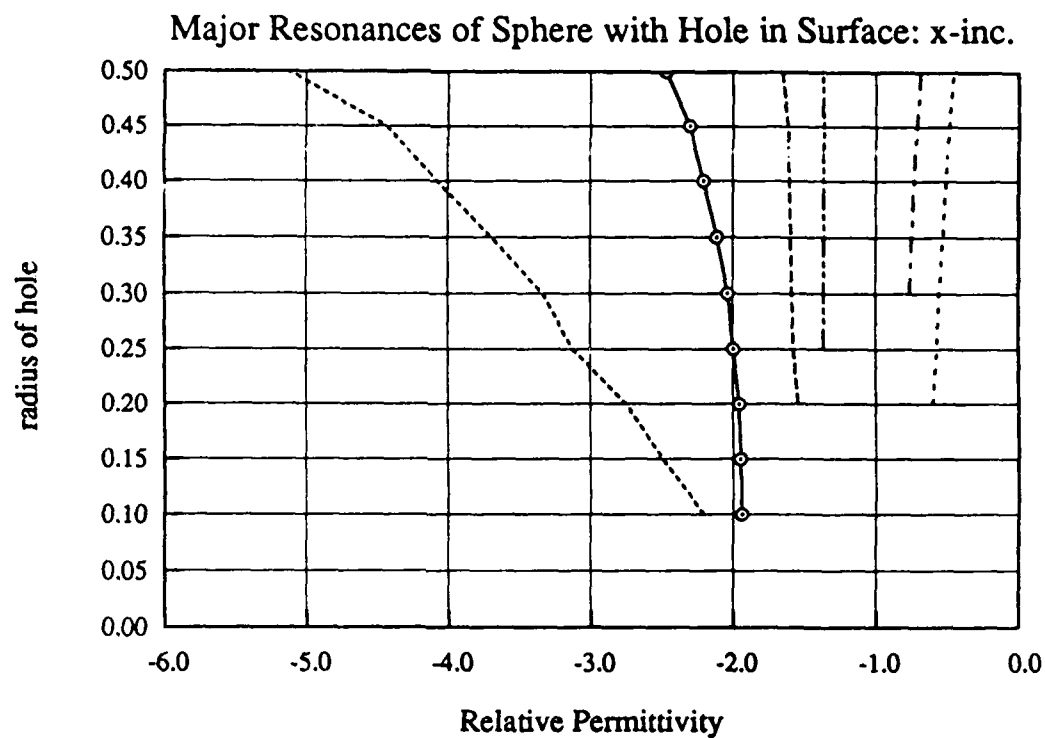


Figure 3.19 — Major Resonances of Spherical Aperture in Sphere as function of Hole Radius.

#### IV. CONCLUSION

A great deal can be learned about small particle absorption with the use of calculated near fields and polarizability tensor elements (as a function of  $\epsilon_r$ ) for different shapes. The shape effects can be quite striking for materials that have bulk permittivities with negative real parts and small ( $< 3$  or so) imaginary parts. Gold in the visible is one such material and we used it extensively in our calculations.

The model of the polarizability tensor elements is very simple and allows clear, physical interpretation of its few free parameters, while fitting our numerically-generated data quite well.

Extensive work still remains in a number of areas, included in these are:

- (1) Finding better ways of choosing the "major" resonances of a particle.
- (2) Understanding the variation of resonance position and strength with geometry, for each family of shapes.
- (3) Understanding the near and internal field structure near a resonance.

Work is continuing on these and other topics.

#### BIBLIOGRAPHY

- Abramowitz, M. and Stegun, I. A. (1964), *Handbook of Mathematical Functions*. National Bureau of Standards.
- Bohren, C. F. and Huffman, D. R. (1983), *Absorption and Scattering of Light by Small Particles*, Wiley, NY.
- Nelson, D. F. (1979), *Electric, Optic, and Acoustic Interactions in Dielectrics*, (esp. Ch. 9) John Wiley and Sons, New York.
- Physik Daten Part II (1981), Fachinformationzentrum Energie, Physik, Mathematik, GMBH, Karlsruhe.
- Senior, T. B. A. and Ahlgren, D. J. (1972), The Numerical Solution of Low Frequency Scattering Problems. *Rad Lab Report*, 103630-9-T.
- Senior, T. B. A. (1976), Low-Frequency Scattering by a Dielectric Body. *Radio Sci*, 11, 477.
- Weil, H. (1986), Surface Roughness, Clustering and Material Effects in Absorption and Scattering by Electrically Small Particles. *Proceedings of the 1985 Scientific Conference on Obscuration and Aerosol Research*, CRDEC-SP-86019, p. 547.